Electronic Properties of Printed Nanoparticulate Silicon

Sara Abdelazeem Hassan Abass

A thesis submitted in fulfilment of the requirements

for the degree of Masters in Science

in the Department of Physics

University of CapeTown

August 21, 2011

Declaration

I know the meaning of plagiarism and declare that all of the work in the document, save for that which is properly acknowledged, is my own.

---------- ----------

Abass Abdelazeem Hassan Sara Date

Abstract

Printed silicon is an award-winning technology in the development of a large area of flexible electronics. The potential applications for printed electronic products range from solar cells and animated billboard posters to packaging and smart fabrics. In an investigation of the fundamental properties of printed nanoparticulate silicon composites, layers were screen printed and successfully characterised to establish their electrical performance using a state of the art Hall Measurement System (HMS). The printable semiconductor inks were formulated by mixing silicon nanoparticles, produced by high energy milling, with an acrylic screen printing polymer binder in varying particle to binder ratios. Hall measurements were performed on the printed layers for variable field between 0 and 1 Tesla at room temperature, using a four point system based on the van der Pauw geometry.

In order to explore properties of the nanoparticulate silicon composite a magnetoconductivity tensor model was developed and applied to extract parameters governing the electrical properties of the material. Sheet carrier concentrations and mobilities for the printed material were obtained and compared with those for bulk doped crystalline silicon, and compressed powder pellets characterised using the same HMS. All the layers showed at least two carrier types. The effect of particle loading and temperature on the electrical properties was also investigated. Particle loading was found to have an influence on the sheet resistivity and carrier concentration of the printed nanoparticulate silicon. Carrier concentration increased with an increase in temperature. Although carrier concentrations are generally low, their mobility was found to be comparable to or even better, than similar classes of semiconductor materials.

Contents

1. Introduction

The study of semiconductors dates back to the early nineteenth century [1]. This class of materials includes silicon (Si), germanium (Ge), gallium arsenide (GaAs) and indium phosphide (InP). Of these, silicon is by far the dominant and most important material for fabrication of electronic devices, such as transistors and solar cells [2, 3]. Silicon is used in its crystalline and amorphous phases, as well as in the form of a nanocrystalline material. In this thesis a new class of nanostructured semiconductor material based on silicon nanoparticles will be investigated. Materials with structural elements, such as clusters, crystallite and grains with dimensions less than 100 nm are classified as nanostructured materials [4, 5]. Nanostructured materials have received much attention because of their unique electrical and optical properties [5, 6], where silicon is no exception. Printed nanoparticulate silicon electronics is a combination of silicon nanotechnology with everyday printing methods, which aims to produce environmentally friendly, disposable devices with high efficiency and small size [7]. In this thesis the production of silicon nanoparticles produced by high energy mechanical milling of bulk silicon is described. The silicon nanopowder was used to produce inks using organic binders. The focus of this work is on the electronic properties of the printed layer formed from the nanoparticulate silicon ink.

The thesis is divided into seven chapters. After the introduction, chapter 2 presents the description of the structural aspects of semiconductors, and their electrical properties. Chapter 3 is concerned with the theoretical description of the Hall effect and the van der Pauw technique. The basis for the multi carrier model treatment as well as the application of the magnetoconductivity tensor are also discussed. These models were used to analyze the experimental findings in chapter 5. In chapter 4, material synthesis, sample preparation techniques and the milling procedure are presented along with the method of ink formulation and screen printing. In this chapter, the Hall effect measurement system and the set-up employed to characterise the layers are also discussed. Chapter 6 presents a unified discussion of all results and the final chapter, chapter 7, summarises the conclusions of this work.

2. Semiconductors

Materials can be classified according to their electrical properties, as conductors, insulators and semiconductors. A conductor is a material that offers very little resistance to the flow of current, and its conductivity is between 10^6 and $10^4(\Omega cm)^{-1}$ [8]. Insulators are materials that almost completely do not allow the flow of current, and typically their conductivity is less than $10^{-8}(\Omega cm)^{-1}$ [9]. At room temperature, a semiconductor conducts electricity more easily than an insulator, but less readily than a conductor. Semiconductors are insulators at absolute zero of temperature, and their conductivity increases as temperature increases [10]. Thus, a semiconductor can be said to exhibit properties between a conductor and insulator.

When atoms are brought together to form a molecule or solid structure, their individual atomic energy levels split to form a band of allowed energy levels. These energy bands may or may not overlap, depending on the shell structure of the atoms, the relative strength of their atomic bonding, and their geometric arrangement. The highest fully occupied band is referred to as the valence band (VB), while the lowest energy band with unoccupied states is referred to as the conduction band (CB) [11]. Materials with partially filled bands or overlapping valence and conduction bands are metals. In the case of semiconductors and insulators, the valence band is completely filled and separated from the conduction band by an energy gap E_g, as shown in Fig. 2.1. The difference between semiconductors and insulators is that in semiconductors the energy gap is small enough (0.5 eV $\leq E_g \leq 3.0$ eV) for electrons to be thermally excited into the conduction band at normal temperatures [11].

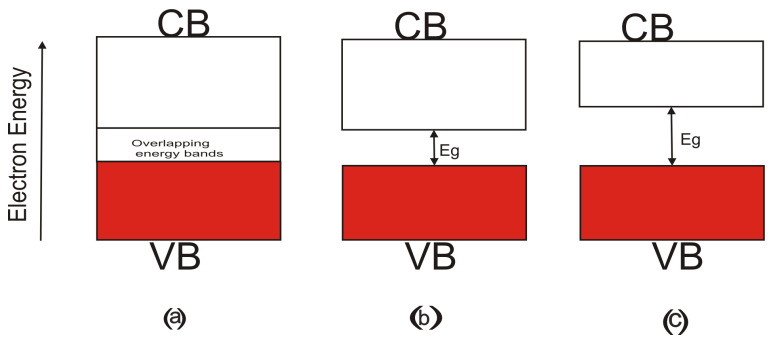

Fig. 2.1: Energy band gap diagrams for (a) conductors, (b) semiconductors and (c) insulators. In (a) the conduction and valence bands overlap while in (b) and (c), there is an energy gap.

Semiconductor properties can be found in the elements of group IV of the periodic table, which consists of carbon, silicon, and germanium, and may also be obtained by a combination of elements of group III and group V, such as GaAs [12]. Most studies of semiconductors have focused on Si and Ge because of their applications in electronic devices.

All elemental semiconductors crystallise in the diamond structure [13, 14]. The diamond structure is a face-centered cubic (fcc) lattice with a basis of two atoms, such that each atom is surrounded by four neighbouring atoms, as shown in Fig. 2.2.

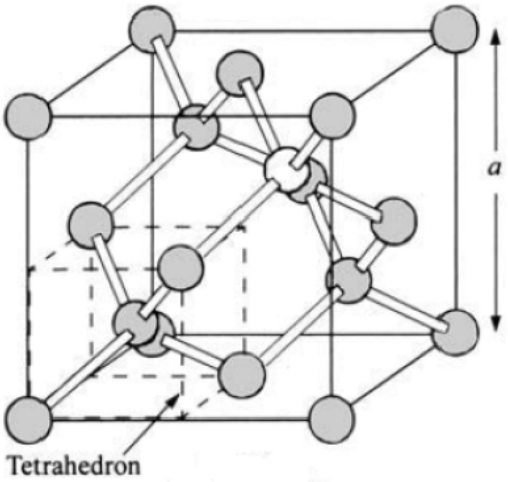

Fig. 2.2: The silicon unit cell, showing the tetrahedral bonding arrangement, a is the fcc lattice parameter [15].

2.1 Band Structure

The energy band structure of crystals varies from one material to another. The energy states in a semiconductor are split to form the valence and conduction bands. In the conduction band there are unoccupied energy levels into which electrons can move. When the temperature is increased, some electrons move from a lower energy level to a higher level. This movement could also be due to the effect of an applied electric field. Electrons in this band are called conduction electrons. In semiconductors the conduction band does not contain any electrons in the ground state, but is partially occupied at high temperature [16]. The missing electrons in the valence band form holes, which are effectively carriers of positive electric charge [16]. The band structure of a semiconductor is shown in Fig. 2.3. At a sufficiently low temperature the valence band is completely filled, and the conduction band is empty of electrons.

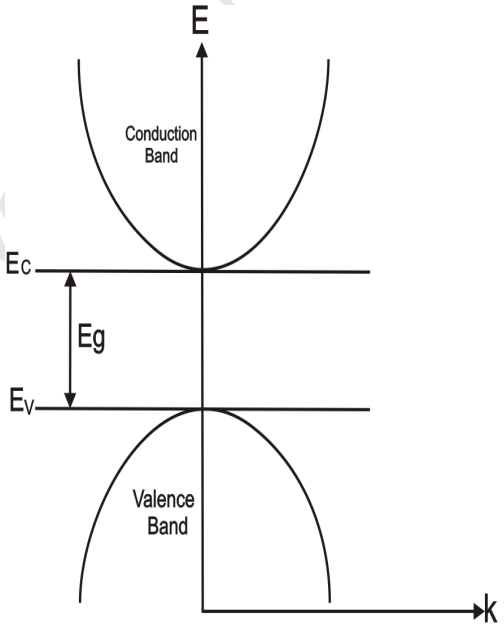

Fig. 2.3: Band structure of Semiconductors.

Electron states with energies near the bottom of the conduction band behave like free electrons [16]. When acted upon by an applied field, the empty states in the valence band accelerate toward free electrons. Indeed, it is easier to imagine particle states of this type as acting like positive

charges. Such states are called hole states. The energy of a state in the conduction band has the form

$$E(k) = E_c + \frac{\hbar^2 k^2}{2m_e^*} \quad , \tag{2.1}$$

where k is the wave vector and m_e^* the effective mass of the electron, defined as ,

$$m^* \;=\; \hbar^2 \left(\frac{\partial^2 E}{\partial k^2} \right) \quad . \tag{2.2}$$

The energy of the valence band as a function of wave vector k, (Fig. 2.3) may be written as

$$E_v(k) = -\frac{\hbar^2 k^2}{2m_h^*} \quad , \tag{2.3}$$

where m_h^* is the effective mass of the hole, $\hbar$ is Plank's constant.

2.2 Dopant Atoms and Energy Levels

In semiconductor crystals, the balance of the number of electrons and holes can be changed by introducing a small amount of impurity atoms having one more or one less valence electron. These impurities are injected into the crystal structure to create what is called a doped or extrinsic semiconductor. If the impurity has one less valence electron, there will not be enough electrons to fill in the valence band. There is thus an excess of holes. This excess of holes increases the normal concentration of the holes, so they become the majority charge carriers. Such materials are referred to as *P*-type semiconductors.

If the impurity has one more valence electron, the electrons in the ground state fill up the valence band, and the extra electron will reside in a discrete energy level created in the energy gap. This level is close to the conduction band where it will enhance the conductivity of the semiconductor. In such materials the current is mainly due to the movement of electrons. These doped semiconductors are called *N*-type semiconductors .

2.2.1 Concentration of Holes and Electrons in Intrinsic Semiconductors

In a pure semiconductor the concentration of electrons (n) is equal to the concentration of holes (p). Such a concentration is called the intrinsic carrier concentration (n_i) of the semiconductor [10]. The intrinsic carrier concentration can also be a function of the energy required to excite an electron from the valence band to the conduction band. The probability that a given energy state with energy E is occupied by an electron is given by the Fermi-Dirac distribution [15]

$$f_e(E) = \frac{1}{1 + exp((E - E_f)/k_B T)} \quad , \tag{2.4}$$

where k_B is Boltzmann's constant, T the absolute temperature and E_f is the Fermi energy.

Thus, the probability that a given energy state with energy E in the valence band is occupied by a hole is given by

$$f_h(E) = 1 - \frac{1}{1 + exp((E - E_f)/k_B T)} \quad . \tag{2.5}$$

If $f(E)$ represents the probability of state of energy E being occupied, the number of occupied conduction band states are given by [15]

$$n = \int N(E) f(E) dE \quad , \tag{2.6}$$

where $N(E)$ is the density of states. If the density of states in the conduction and valence band is calculated, the concentration of electrons in the conduction band is [15]

$$n = N_c exp(-(E_c - E_f)/kT) \quad , \tag{2.7}$$

and the concentration of holes in the valence band is

$$p = N_v exp(-(E_f - E_v)/kT) \quad , \tag{2.8}$$

where, E_v is the energy of the top of the valence band, E_c is the energy of the bottom of the conduction band, N_c and N_v are the effective density of states in the conduction and valence bands respectively.

The intrinsic carrier density n_i is thus equal, because the electrons in the conduction band are due to exciting a hole in the valence band [17],

$$n_i \;=\; n = p \qquad , \tag{2.9}$$

and therefore

$$n_i^2 \;=\; np \qquad .$$

2.2.2 Extrinsic Semiconductors

When a semiconductor is doped with donor or acceptor impurities, impurity energy levels are introduced into the forbidden band gap of that semiconductor [10]. These impurity levels may be either donor levels, which are just below the conduction bands, or acceptor levels, which are just above the valence bands [15]. In an extrinsic semiconductor a specific impurity element is added in controlled amounts. The impurity concentration will determine the conductivity of the sample and the type of charge carrier. Extrinsic semiconductors can therefore be *N*-type or *P*-type, depending on the type of impurity atoms present, as discussed below.

N-type Silicon

N-type doping is achieved by adding to the silicon a group V element such as phosphorus, arsenic or antimony. The group V element has five valence electrons, four of which will contribute to the covalent bonding with the silicon atoms, as shown in Fig. 2.4. At a low temperature, the fifth electron occupies a donor level in the band gap and is bound to the phosphorus atom. At a higher temperature by thermal ionisation, it can move into the conduction band. The electron in the conduction band can now move through the crystal and the positively charged ion is fixed in the crystal. This type of impurity atom donates an electron to the conduction band, and so is called a donor impurity. The resulting material is referred to as an *N*-type silicon.

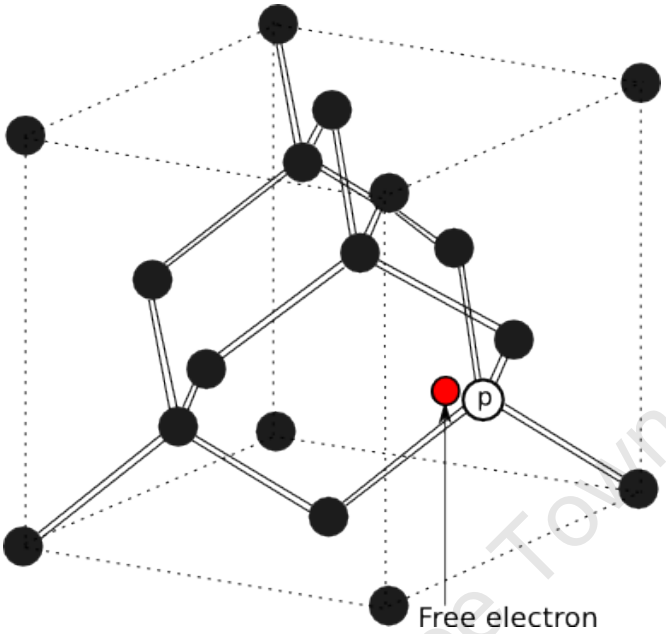

Fig. 2.4: The silicon unit cell with phosphorus dopant atom, modified from [18].

P-type Silicon

P-type doping is achieved by adding a group III element, such as boron, as a substitutional impurity atom in the silicon structure. The group III element has three valence electrons, which are all taken up in the covalent bonding, as shown in Fig. 2.5. For an electron to fill the vacant state created by the presence of the boron atom, its energy must be greater than that of the valence band, since the net charge state of the boron atom would now be negative. When the boron atom is ionised, it accepts an electron from the valence band. The acceptor atom can therefore generate holes in the valence band without generating an electron in the conduction band. This type of semiconductor material is referred to as a *P*-type silicon.

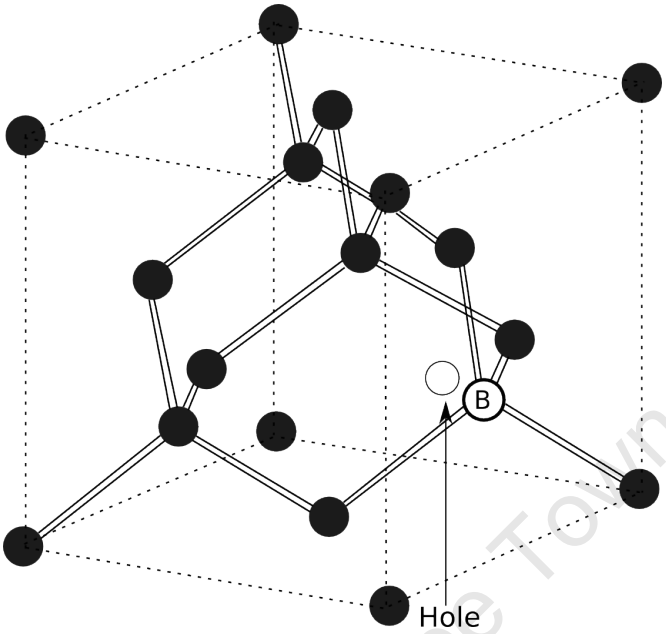

Fig. 2.5: The silicon unit cell with boron dopant atom, modified from [18].

2.3 Electronic Properties of Semiconductors

Mobility, conductivity and resistivity are the most important electrical properties which distinguish semiconductor materials from each other [19]. A brief discussion of these electronic properties of semiconductors is given below.

Mobility

The drift mobility μ_d is defined as the proportionality constant between an applied electric field E and the drift velocity v_d of a charge carrier [18].

$$\mu_d = \frac{v_d}{E} \quad . \tag{2.10}$$

Mobility is positive for both electrons and holes, although their drift velocities are in opposite directions in a given electric field. Writing μ_e or μ_h denotes the electron or hole mobility respectively. Table 2.1 shows the electron and hole mobilities for some semiconductors.

Table 2.1: Electron and hole mobilities at room temperature of the different semiconductors [2].

Material	μ_e(m^2/Vs)	μ_h(m^2/Vs)
Diamond	0.20	0.21
Si	0.145	0.037
Ge	0.390	0.180
Sn	0.294	0.299
AlAs	0.030	0.020
GaAs	0.840	0.045

Resistivity

The resistivity ρ of a material is a measure of how strongly it opposes the flow of electric current passing through it and is the inverse of the conductivity σ. If a material has a low resistivity, it means that it readily allows the flow of electric current through it. For a particular sample, the electrical resistivity ρ can be determined from its resistance R as

$$\rho = \frac{RA}{\ell} \quad , \tag{2.11}$$

where ℓ is the length of the piece of material, and A is its cross-sectional area. In a metal, electrical resistivity increases with temperature, while in semiconductors it decreases.

For semiconductors with both electrons and holes as carriers, the drift current density J under an applied field E is given by

$$J = \sigma E \quad ,$$

where, in terms of the current I and voltage V, $J = I/A$ and $E = V/\ell$.

Conductivity

The conductivity σ is given in terms of the carrier concentration and mobility as

$$\sigma = \frac{1}{\rho} = e(\mu_n n + \mu_p p) \quad , \tag{2.12}$$

where n is the concentration of electrons and p the concentration of holes. If $n >> p$, as in *N*-type semiconductors,

$$\rho = \frac{1}{e\mu_n n} \quad , \tag{2.13}$$

and

$$\sigma = e\mu_n n \quad . \tag{2.14}$$

3. Theory of the Hall Effect

3.1 Introduction

The Hall effect, discovered in 1879 by Edwin H. Hall, is used to study the physics of charge transport in metals and semiconductors [15]. It is the basis of many practical applications, such as magnetic field measurements and in devices such as position and motion detectors [15]. More importantly, through the Hall effect, it was possible for the first time, to determine the sign of charge carriers in a conductor. Even today, Hall effect measurements continue to be a useful technique for characterising the electrical transport properties of metals and semiconductors [20].

3.2 Hall Effect in Materials

When an electric current passes through a sample placed in a magnetic field, a potential proportional to the current and the magnetic field is developed across the material in a direction perpendicular to both the current and the magnetic field. Consider a conducting slab, shown in Fig. 3.1, with length L in the x direction, width W in the y direction, and thickness t in the z direction. Furthermore, if it is assumed that current I_x flows in the positive x direction while the sample has charge carriers of charge $q = \pm e$ (positive or negative charge), charge carrier number density n, defined as the number of carriers per unit volume, and charge carrier drift velocity v_x, then [18],

$$I_x = J_x W t = n q v_x W t \quad . \tag{3.1}$$

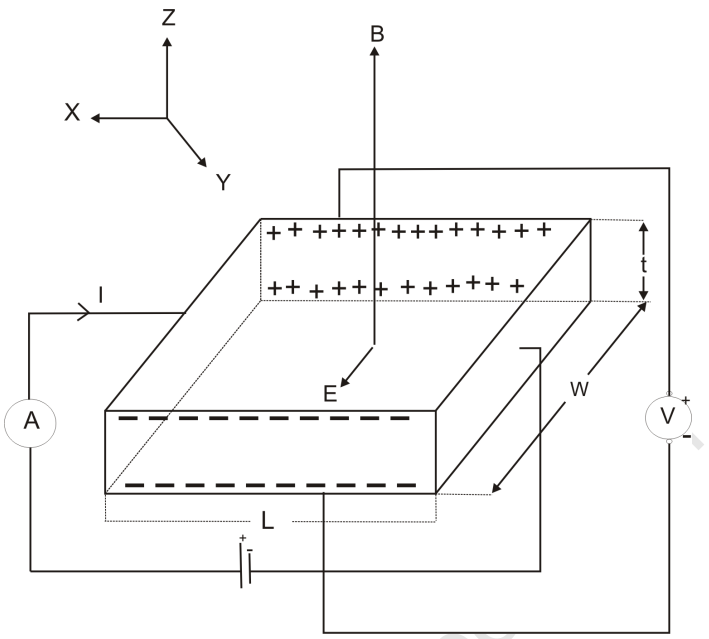

Fig. 3.1: Principle of a Hall effect measurement, showing the arrangement of the applied field and current with respect to the conductor, and the measurement of the Hall voltage [18].

The drift velocity is the average velocity of the charge carriers over the volume of the sample, since under the influence of an applied electric field, there will be a net transport of carriers along the length of the sample. The current density J_x is the charge density nq times the drift velocity v_x, and the current I_x is the product of the current density, and the cross-sectional area of the sample Wt.

The current I_x is therefore caused by applying an electric field (E_x) along the length of the sample. In the case where the current density is directly proportional to the applied field, the material obeys Ohm's Law, which may be written as [18]

$$J_x = \sigma E_x \quad , \tag{3.2}$$

where σ is the conductivity of the sample. If there is a magnetic field (B) with a component perpendicular to the plane of the sample, the charge carriers will experience a Lorentz force [12]

$$\vec{F} = q\vec{E} + q(\vec{v} \times \vec{B}) \quad , \tag{3.3}$$

that will deflect them towards one side of the sample. The deflection causes an accumulation of

charges along one side of the sample, which creates a transverse electric field E_y that counteracts the force of the magnetic field. In a steady state, the electric force will then be equal to the magnetic force, that is,

$$qE_y = qv_xB_z \quad . \tag{3.4}$$

Hence, there will be no net flow of charge in the y direction. The electric field in the y direction is called the Hall field (E_H), which can, however, be expressed in terms of a potential difference, known as the Hall voltage (V_H), which can be measured. It is given by

$$V_H = E_HW = v_xB_zW \quad . \tag{3.5}$$

Substituting equations (3.1) in equation (3.5), we obtain

$$V_H = \left(\frac{1}{nq}\right)\frac{I_xB_z}{t} \quad . \tag{3.6}$$

Since we measure V_H, and B, I, W and v_d are predetermined inputs, one can calculate n by inverting equation (3.6). Then, the Hall coefficient R_H is defined as

$$R_H = \frac{V_Ht}{I_xB_z} \quad . \tag{3.7}$$

Comparison with equation (3.6) yields the Hall coefficient in terms of the carrier density,

$$R_H = \frac{1}{nq} \quad . \tag{3.8}$$

However, if the thickness t of the materials is unknown, the layer or sheet carrier density ($n_s = nt$), is used instead of the bulk carrier density (n),

$$n_s = \frac{IB}{qV_H} \quad . \tag{3.9}$$

The Hall coefficient is negative if the majority carriers are electrons ($q = -e$), and positive if the majority carriers are holes ($q = +e$). However, in real materials,

$$R_H = \frac{r_H}{n|q|} \quad , \tag{3.10}$$

where r_H is known as the Hall factor or scattering factor, and is a material constant, of the order of unity [15]. The Hall mobility determined by using (2.13) and (3.8) is thus,

$$\mu = \frac{R_H}{\rho} \quad . \tag{3.11}$$

In a single crystal the Hall mobility is equivalent to the drift mobility [15].

In a semiconductor there are both negative charge carriers (electrons) and positive charge carriers (holes). In this case, where charge is carried by both electrons and holes, the expression for the Hall coefficient in terms of the hole and electron mobilities, μ_p and μ_n, respectively, and carrier concentrations,n and p, is [21, 15]

$$R_H = \frac{p\mu_p^2 - n\mu_n^2}{|q|(p\mu_p + n\mu_n)^2} \quad . \tag{3.12}$$

From equation (3.12), it is clear that the Hall coefficient depends on both the mobility and the concentrations of holes and electrons.

The description of the Hall effect given above represents only a first order approximation to the complete transport situation in materials. Often only a single magnetic field measurement is used to determine the Hall coefficient [22]. In this case, the parameters extracted are limited to the dominant, or majority, carrier type for which the conduction is assumed to take place in a single band [22].

Conduction in a single band is characterised by having a single relaxation time and a single value of mobility representing a single carrier type [22]. However, in practice, materials may have complex conduction band structures with a non spherical Fermi surface, in the case of metals, or a non parabolic dispersion curve [22] for semiconductors. Under such conditions the relaxation time and the mobility are not unique [22]. The corresponding electronic structure is referred to as a multi band structure with multiple carrier types [23, 24]. For such a multicarrier system, the simple description of the Hall effect given above is not adequate, and could even be misleading [23].

3.3 Magnetoconductivity Tensor

An alternative method to analyse the Hall effect is the determination of the magnetoconductivity tensor from variable field measurements, which helps to determine parameters such as carrier density and carrier mobility for a given material or device with a multicarrier or multiband structure [23].

The magnetoconductivity tensor, in some sense, is a mathematical object that enables the expansion of equation (3.2) to its components, so that it represents the more general and realistic situation.

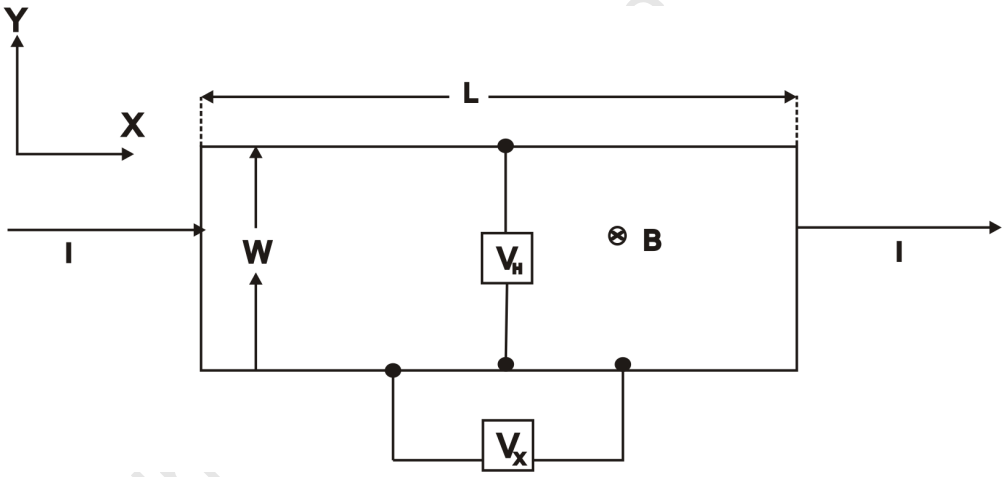

Fig. 3.2: Schematic of a magnetoconductivity tensor measurement.

Consider a sample of length L, width W and thickness t placed in a magnetic field with an applied current I_x along the x -axis as shown in Fig 3.2. In uniform isotropic materials the resistivity is a symmetric tensor with components given by

$$\rho_{xx} = \frac{V_x}{I}\frac{W}{L}t \quad , \tag{3.13}$$

and

$$\rho_{xy} = \frac{V_H}{I}t \quad . \tag{3.14}$$

Ohm's law is given in tensor form as

$$J_i = \sigma_{ij}E_j \quad , \tag{3.15}$$

or in terms of the resistivity tensor

$$E_i = \rho_{ij}J_j \quad , \tag{3.16}$$

where i, j, k are x, y, z the Cartesian coordinates respectively. Both σ_{ij} and ρ_{ij} are a function of the magnetic field B, that is, $\sigma_{ij} = \sigma_{ij}(B)$ and $\rho_{ij} = \rho_{ij}(B)$. Equation (3.15) may be then expanded as a matrix equation

$$\begin{bmatrix} J_x \\ J_y \\ J_z \end{bmatrix} = \begin{pmatrix} \sigma_{xx} & \sigma_{xy} & \sigma_{xz} \\ \sigma_{yx} & \sigma_{yy} & \sigma_{yz} \\ \sigma_{zx} & \sigma_{zy} & \sigma_{zz} \end{pmatrix} \begin{bmatrix} E_x \\ E_y \\ E_z \end{bmatrix} \quad . \tag{3.17}$$

The relation between the conductivity coefficients σ_{ij}, in equation (3.15) and resistivity coefficient ρ_{ij}, in equations (3.16) is

$$\rho_{ij}\sigma_{jk} = \delta_{ik} \quad , \tag{3.18}$$

where

$$\delta_{ik} = \begin{cases} 1 & : \quad i = k, \\ 0 & : \quad i \neq k. \end{cases}$$

Thus equation (3.18) may be written in matrix form as

$$\begin{pmatrix} \rho_{xx} & \rho_{xy} & \rho_{xz} \\ \rho_{yx} & \rho_{yy} & \rho_{yz} \\ \rho_{zx} & \rho_{zy} & \rho_{zz} \end{pmatrix} \begin{pmatrix} \sigma_{xx} & \sigma_{xy} & \sigma_{xz} \\ \sigma_{yx} & \sigma_{yy} & \sigma_{yz} \\ \sigma_{zx} & \sigma_{zy} & \sigma_{zz} \end{pmatrix} = \begin{pmatrix} 1 & 0 & 0 \\ 0 & 1 & 0 \\ 0 & 0 & 1 \end{pmatrix} \quad . \tag{3.19}$$

When the magnetic field is acting along the z direction, $B = B_z$ [25],

$$\begin{aligned} \sigma_{xx}(B) &= \sigma_{yy}(B) \quad , \\ \sigma_{xy}(B) &= -\sigma_{yx}(B) \quad , \end{aligned} \tag{3.20}$$

and

$$\sigma_{xz}(B) = \sigma_{zx}(B) = \sigma_{yz}(B) = 0 \quad . \tag{3.21}$$

So, in the xy-plane, equations (3.17) and (3.19) are expressed as

$$\begin{bmatrix} J_x \\ J_y \end{bmatrix} = \begin{pmatrix} \sigma_{xx} & \sigma_{xy} \\ \sigma_{yx} & \sigma_{yy} \end{pmatrix} \begin{bmatrix} E_x \\ E_y \end{bmatrix} \quad , \tag{3.22}$$

and

$$\begin{pmatrix} \rho_{xx} & \rho_{xy} \\ \rho_{yx} & \rho_{yy} \end{pmatrix} \begin{pmatrix} \sigma_{xx} & \sigma_{xy} \\ \sigma_{yx} & \sigma_{yy} \end{pmatrix} = \begin{pmatrix} 1 & 0 \\ 0 & 1 \end{pmatrix} \quad . \tag{3.23}$$

This matrix equation can be rewritten explicitly in the form

$$\rho_{xx}\sigma_{xx} + \rho_{xy}\sigma_{yx} = 1, \tag{3.24a}$$

$$\rho_{xx}\sigma_{xy} + \rho_{xy}\sigma_{yy} = 0, \tag{3.24b}$$

$$\rho_{yx}\sigma_{xx} + \rho_{yy}\sigma_{yx} = 0, \tag{3.24c}$$

$$\rho_{yx}\sigma_{xy} + \rho_{yy}\sigma_{yy} = 1. \tag{3.24d}$$

The conductivity tensor components, σ_{xx} and σ_{xy} can be written as [26, 23]

$$\sigma_{xx} = \frac{\rho_{xx}}{\rho_{xx}^2 + (R_H B)^2} = \frac{nq\mu}{1 + (\mu B)^2} \quad , \tag{3.25}$$

$$\sigma_{xy} = \frac{R_H B}{\rho_{xx}^2 + (R_H B)^2} \quad = \quad \frac{nq\mu^2 B}{1 + (\mu B)^2} \quad , \tag{3.26}$$

where n is the carrier concentration, μ is the mobility, and q is the charge of the carrier. ρ_{xx} and R_H are the measured values of longitudinal magnetoresistance and the Hall coefficient respectively.

Equations (3.25) and (3.26) are equally valid for both bulk and sheet parameters, but are based on the assumption that the system contains a single type of charge carrier. For multiple carriers, the conductivities of the individual carrier types are additive. The total conductivity tensor for N different carrier populations is then given by [26]

$$\sigma_{xx} \quad = \quad \sum_i^N \frac{n_i q_i \mu_i}{1 + (\mu_i B)^2} \quad = \quad \sum_i^N \sigma_{xx,i} \quad , \tag{3.27}$$

and

$$\sigma_{xy} \quad = \quad \sum_i^N \frac{n_i q_i \mu_i^2 B}{1 + (\mu_i B)^2} \quad = \quad \sum_i^N \sigma_{xy,i} \quad = \quad B \sum_i^N \mu_i \sigma_{xx,i} \quad , \tag{3.28}$$

where n_i is the density of carrier i, and q_i is the charge of a carrier type i, which may be holes ($q = +e$) or electrons ($q = -e$).

Consequently, a least- squares fit of derived data given by (3.25) and (3.26) to equations (3.27) and (3.28) determines the carrier concentrations n_i and their mobilities μ_i, for a predefined number of carrier types, N.

3.4 Hall Effect Measurements

3.4.1 Sample Geometry

Hall effect measurements commonly use two sample geometries: a long, narrow Hall bar geometry as shown in Fig. 3.3; and a nearly square or circular van der Pauw geometry as shown in Fig.

3.4. Each sample geometry has its own advantages and disadvantages. The Hall bar has a good geometry for performing resistance measurements, since about half of the voltage applied across the sample appears between the voltage measurement contacts. For this reason, Hall bars are commonly used when measuring magnetoresistance or Hall mobility on samples with low resistances [27]. Disadvantages of the Hall bar geometry are that, at least six contacts are necessary to perform mobility measurements. Also the Hall bar width, as well as the distance between the side contacts, is difficult to measure accurately. However, the accuracy can be increased by making contact with the sides of the bar at the end of extended arms [27] as shown in most examples in Fig. 3.3.

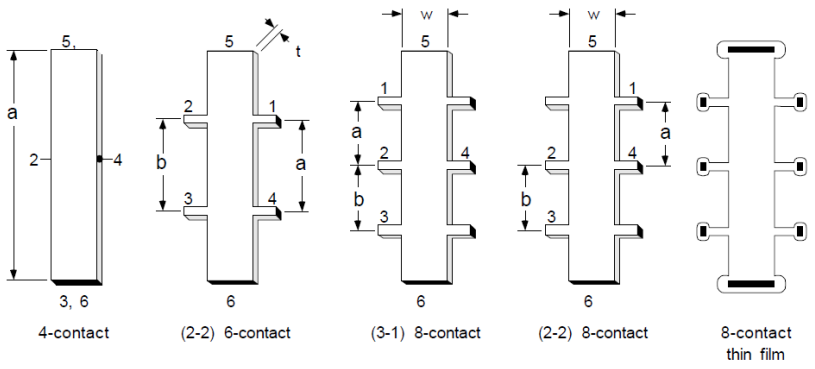

Fig. 3.3: Common Hall bar sample geometries [27].

In contrast, the main advantage of the van der Pauw geometry is that only four contacts are required. Also, there is no need to measure sample widths or distances between contacts. Moreover, simple geometries can be used. Disadvantages are that the measurements take about twice as long as those using the Hall bar geometry, and the errors due to contact size and placement can be significant when using these simple geometries. However, to reduce this error the ratio of the contact size (c) and sample size (L) should be approximately $\frac{1}{6}$ [28]. These geometrical errors are discussed further in Appendix A.

Fig. 3.4 shows several van der Pauw geometries, such as square 3.4(a), circular 3.4(b), clover leaf 3.4(c) and greek cross structures 3.4(d). The most commonly used geometries are the square

and clover leaf, with the main advantage of the clover leaf pattern being its having comparatively large contacts while still retaining relatively low contact size related errors [29].

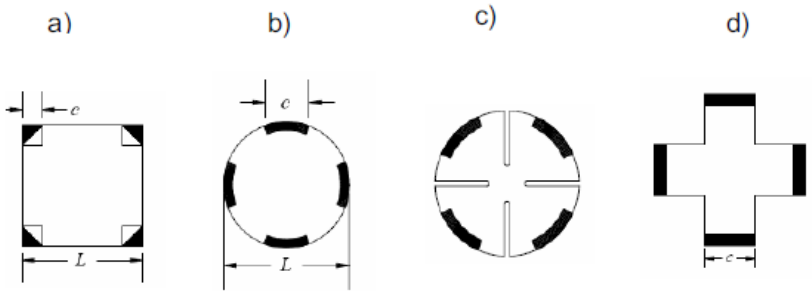

Fig. 3.4: van der Pauw geometries for Hall effect measurements: a) square, b) circular, c) clover leaf, and d) greek cross structures [20].

3.4.2 The van der Pauw Technique

The van der Pauw technique can be used for the determination of the bulk resistivity, as well as the carrier density of bulk materials. However, the main objective is to determine the values of the sheet resistivity R_s and carrier sheet density n_s of a flat sample of arbitrary shape [20, 30]. Measurement using the van der Pauw geometry allows the determination of R_s, through the van der Pauw equation [31],

$$\exp(-\pi\frac{R_A}{R_s}) + \exp(-\pi\frac{R_B}{R_s}) = 1 \quad , \tag{3.29}$$

where R_A and R_B are characteristic resistances which are obtained as

$$R_A = \frac{V_{43}}{I_{12}} \quad , \tag{3.30}$$

$$R_B = \frac{V_{14}}{I_{23}} \quad . \tag{3.31}$$

To obtain R_A, a DC current I_{12} is applied into contact 1 and out of contact 2, and the potential difference V_{43} between contact 4 and contact 3 is measured, as shown in Fig. 3.5(a). Similarly,

to obtain R_B, a current I_{23} is applied into contact 2 and out from contact 3 while measuring the voltage V_{14} between contact 1 and contact 4 as shown in Fig. 3.5(b).

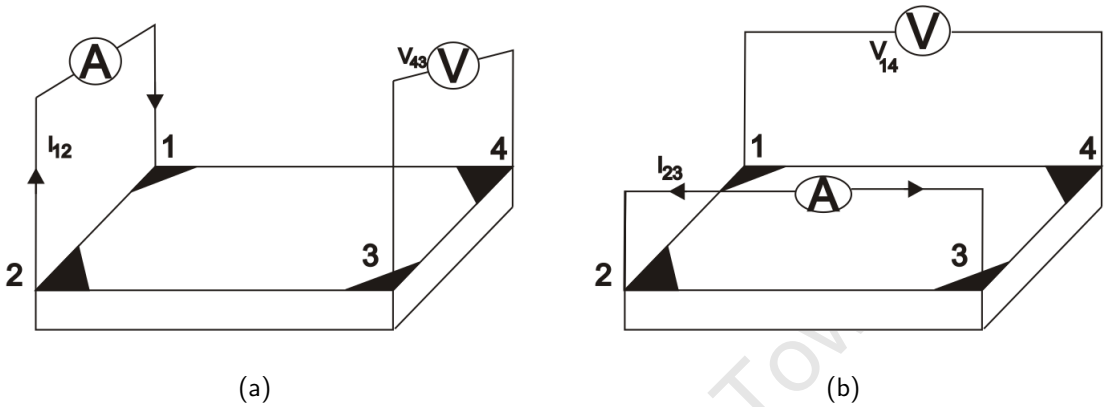

Fig. 3.5: Geometry of the van der Pauw technique for measurement of sheet resistivity [20].

Equation (3.29) can be solved numerically to obtain R_s. This equation has a unique solution for sheet conductivity because R_A and R_B are both positive [32]. More details can be found in the original work of van der Pauw [27, 33]. If the sample thickness t is uniform, the bulk resistivity is obtained simply by using

$$\rho = R_s t \quad . \tag{3.32}$$

The Hall voltage measurement involves measuring the voltage across a sample perpendicular to a constant current I and at a constant magnetic field B perpendicular to the plane of the sample as shown in Fig.3.6.

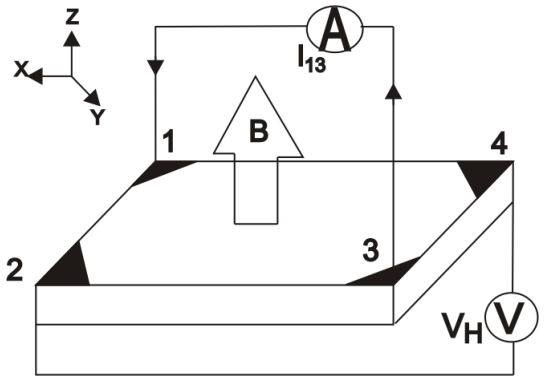

Fig. 3.6: Geometry of the van der Pauw technique for the measurement of the Hall voltage [20].

The Hall voltage V_H is measured between contacts 2 and 4 when the current I passes through contact 1 to contact 3. The sheet carrier density n_s can then be calculated from the known values of I, B and q by the relation

$$n_s = \frac{IB}{qV_H} \quad . \tag{3.33}$$

In practice, to improve accuracy an average of all permutations of measurements are used as described below.

3.4.3 Calculation of the Resistivity and Hall Coefficient

In the context of calculating the sheet resistivity we may define $R_{ij,kl} = V_{kl}/I_{ij}$, where the first two pairs of indices indicate the direction of the current while the second pair refer to the potential difference [27, 28]. It is also noted that due to the symmetry of permuting any pair of indices, we have

$$\begin{aligned} R_{12,43} &= R_{21,34} \quad , \\ R_{23,14} &= R_{32,41} \quad , \\ R_{34,21} &= R_{43,12} \quad , \\ R_{41,32} &= R_{14,23} \quad . \end{aligned} \tag{3.34}$$

Furthermore, substituting the reciprocity condition [20], $R_{12,43} = R_{34,21}$ and $R_{23,14} = R_{41,32}$, into equation (3.34) we have

$$R_{12,43} + R_{21,34} = R_{43,12} + R_{34,21} \quad , \tag{3.35}$$

and

$$R_{23,14} + R_{32,41} = R_{14,23} + R_{41,32} \quad . \tag{3.36}$$

In order to minimise the possible errors in the measurements, the following geometry-based definitions are used to define the resistance and subsequently resistivity,

$$R_A = \frac{R_{12,43} + R_{21,34} + R_{43,12} + R_{34,21}}{4} \quad , \tag{3.37}$$

and

$$R_B = \frac{R_{23,14} + R_{32,41} + R_{14,23} + R_{41,32}}{4} \quad . \tag{3.38}$$

So, the resistivity ρ and sheet resistance R_s can be calculated by solving the van der Pauw equation [31]. We obtain

$$\rho = \frac{\pi t}{\ln 2}\left\{\frac{R_{21,34} + R_{32,41}}{2}\right\} f \quad , \tag{3.39}$$

where t is the sample thickness and f is the van der Pauw correction factor which is a function of the ratio $\frac{R_{12,43}}{R_{23,14}}$ [28, 29]. Then,

$$\frac{(R_{12,43}/R_{23,14}) - 1}{(R_{12,43}/R_{23,14}) + 1} = f\, arcosh\left\{\frac{exp(\ln 2/f)}{2}\right\} \quad . \tag{3.40}$$

Denoting the ratio of resistances $\frac{R_{12,43}}{R_{23,14}}$ as Q, equation (3.40) reduces to

$$\frac{Q-1}{Q+1} = \frac{f}{\ln 2} cosh^{-1}\left\{\frac{1}{2} exp\left[\frac{\ln 2}{f}\right]\right\} \quad . \tag{3.41}$$

The van der Pauw correction factor f may be regarded as a measure of symmetry of the sample. For a perfectly symmetric sample $f = 1$ [34].

It is worth noting that it is useful to average ρ by including the remaining two contact permutations, and also reversing the current for all four permutations, thus ρ becomes [28]

$$\rho = \frac{\pi t}{\ln 2}\frac{1}{8}\left[(R^+_{21,34} - R^-_{21,34} + R^+_{32,41} - R^-_{32,41}) f_A \right. \\ \left. + (R^+_{43,12} - R^-_{43,12} + R^+_{14,23} - R^-_{14,23}) f_B\right] \quad , \tag{3.42}$$

where $R^+_{ij,kl}$ denotes a Hall resistance measured while a positive current is passing through, and $R^-_{ij,kl}$ the corresponding Hall resistance with reversing the current. f_A and f_B are geometrical factors determined from Q_A and Q_B, respectively where,

$$Q_A = \frac{R_{21,34} - R_{12,34}}{R_{32,41} - R_{23,41}} \quad , \tag{3.43}$$

$$Q_B = \frac{R_{43,12} - R_{34,12}}{R_{14,23} - R_{41,23}} \quad . \tag{3.44}$$

To see how the Hall coefficient is measured, consider the sample in Fig. 3.6. From equation (3.7) it can be seen that, for a constant applied magnetic field B_z, R_H is proportional to the quotient V_H/I_x. The Hall coefficient is then given by the following expression [8]

$$R_H = \frac{t}{B}\left(\frac{R_{31,42}+R_{42,13}}{2}\right) \quad . \tag{3.45}$$

Similar to the average used in determining the resistivity ρ, the Hall coefficient may be obtained as

$$R_H = \left(\frac{t}{8B}\right)\left[R^{+}_{42,13}(+B) - R^{-}_{42,13}(+B) + R^{+}_{31,42}(+B) - R^{-}_{31,42}(+B) + R^{+}_{24,13}(-B) - R^{-}_{24,13}(-B) + R^{+}_{13,42}(-B) - R^{-}_{13,42}(-B)\right] \quad , \tag{3.46}$$

where $(+B)$ and $(-B)$ represent the magnetic field in the opposite directions. Once the Hall coefficient is known, the carrier concentration n can be calculated through equation (3.8).

4. Experimental Methods

4.1 Nanoparticle Production and Sample Preparation

4.1.1 Background

Nanomaterials are materials with at least one dimension of less than 100 nm [4]. This dimension refers to the thickness of a layer for one dimensional (1-D) nanomaterials such as films and coatings [6]. Two-dimensional (2-D) nanomaterials are those in which the width (or diameter) is in the nanometre range. Examples include rod-like or filamentary nanomaterials, such as carbon nanotubes and nanowires [6]. Three-dimensional (3-D) nanomaterials have their dimensions in all directions in the order of nanometres and include nanoparticles, quantum dots, and hollow spheres [35]. The silicon particles produced by mechanical milling investigated in this work, are an example of a three-dimensional nanomaterial. When printed, a nanoparticulate layer is formed, which represents a three-dimensional nanostructure material.

Nanoparticles can be produced using two general approaches: "bottom-up" methods or "top-down" methods [4, 36, 37]. In principle, bottom-up synthesis involves the production of a material by building the nanostucture from atoms, molecules or a cluster of materials. Thus, the bottom-up approach is an additive process in which the final material is produced by the build up of smaller units [37, 38]. Top-down processes involve breaking down a bulk material into smaller units having final dimensions in the nanometre range. In this work, a top-down process in the form of the mechanical attrition of bulk silicon, was utilised to produce a powder with nano scale sized particles [7].

4.1.2 Nanoparticle Production

Czochralski grown silicon wafers were used as feedstock for a milling process to produce nanoparticles. *N*-type silicon wafers were phosphorus doped and *P*-type silicon wafers were boron doped [7]. The *N*-type and *P*-type wafers both had a bulk resistivity of $0.01 - 0.05\ \Omega$cm as specified by the manufacturer. High energy mechanical milling was performed using an 800 W Siebtechnik laboratory orbital pulverizer (Scheibenschwingmühle), with a set of four pots each containing a 52100 chrome steel pestle and mortar [7]. Fig. 4.1 shows the photograph of a four pot milling station, used for the milling of *N*-type and *P*-type wafers.

Fig. 4.1: A four-pot milling station.

The operation of the mill involved a forceful shaking in two directions of four pots mounted on a four way adaptor plate shown in Fig. 4.1. As the pots are shaken, the inertia of the pestles causes them to hit against the container walls, grinding the sample in the process. Prior to milling the silicon wafers were weighed out using a Vibra AFR220E electronic balance and were separated into four batches each of average mass of 27 g. The weighed wafers were stored in paper envelopes. Before the milling process, the pots and pestles were first cleaned by milling clean quartz in each pot for a period of between 10 to 15 minutes. This process served to remove solid contaminants from the walls of the pots. The pots were then emptied and blown with

compressed air to remove the quartz dust. The pots and pestles were then washed with acetone using lint free paper, and then rinsed with ethanol.

The wafers were then loaded into the pots, and broken into fragments varying from centimetre to millimetre dimensions, using the pestles. Pots were then covered with their lids, mounted onto the 4- way adaptor and clamped into position, before the milling process started. Milling was carried out continuously for 5 hours. Once the milling was completed, the pots were allowed to cool down for about one hour before transferring the milled powder to plastic containers. Other studies [39] have shown that these particles have a log- normal size distribution, with a median size around 80 nm, and to be polycrystalline with a grain size of $10 - 15$ nm.

4.1.3 Ink Preparation

Screen printable ink was produced by mixing the silicon nanoparticles with a suitable binder. The binder used was an acrylic screen printing base obtained commercially from Marchem (pty) Ltd, Cape Town, South Africa. This binder is a commonly used polymer binder in the screen printing industry [7, 40]. As a solvent propylene glycol was used to adjust the rheology of the ink.

The ink preparation was performed through different steps. All equipment including spatulas and glass mixing bowls were cleaned with acetone, and then ethanol using lint free paper. The silicon powder was transferred to a clean glass and weighed using the AFR220E electronic balance. A printable ink composition was produced by successively adding powder and solvent and stirring the components together.

Suitability of the ink for printing was determined using the contact angle technique [41, 42], which was used in this work to quantify the surface tension. The contact angle θ is defined as the angle between the substrate and the tangent to the surface of the drop. The best printable ink for this work corresponded to contact angles on glass ranging between 50° and 60° .

Several inks were produced from *N* and *P*-type silicon nanoparticles. Inks of 88% by weight of

particle to binder ratio for both types of silicon were used to print Hall effect samples in order to determine the electrical properties of the printed layers. In addition, *N*-type inks with different particle loading (88%, 80% and 60%) were also mixed to print nanoparticulate silicon layers to investigate the effect of particle loading on the carrier concentration and mobility.

4.1.4 Screen Printing

Screen printing was used to deposit silver to form the electrical contacts as well as the functional silicon inks prepared, as described above [43]. For the contacts, Luxprint 5000 silver ink supplied by Dupont MCM, UK, was chosen. The substrate used was 80 gm^{-2} plain paper with no pre-treatment. Printing was performed under prevailing ambient conditions of between 22° C to 24° C and relative humidity of 46% to 64%.

Using an ATMA-AT-60PD screen printer, silver ink was printed with a zero off contact setting, squeegee angle of 20° and printing speed of 250 mm.s^{-1}. A double stoke single print mode was used to ensure a uniform printed layer with no pinholes. A squeegee pressure setting of 1.7 mm was used to achieve uniform and reproducible quality of the printed silver layer. For printing silicon inks, an off contact of 0.1 mm, speed of 250 mm.s^{-1} and squeegee pressure setting of 16 mm were used. The silicon inks were printed within 10 to 15 minutes after ink preparation to avoid ageing of the ink and any resulting change in the rheological properties of the ink. The screen tension was measured using a Sefar Tensocheck 100 tensometer before and after each print session to ensure compliance with our requirement of 20 to 25 N/cm.

The silver contacts were allowed to dry, under ambient conditions, for about 18 hours, with the nanoparticulate silicon inks subsequently printed within 24 hours after the silver contacts cured. The average sheet resistivity of the silver layers was determined to be 0.494 ± 0.026 Ω/square, from measurements of the resistance of 30 rectangular layers printed on the same substrates using the screen shown in Fig. 4.2. The layers measured 15 mm $\times$ 10 mm, with an average thickness of 13.84 ± 2.04 μm determined with a micrometer screw gauge. The resistance measurement was

based on a four point system along the sample diagonal using a Keithley 2000 digital multimeter. A sample holder with spring loaded contacts, with a probe diameter of 0.502 ± 0.003 mm (shown in Fig. 4.4 with a van der Pauw Hall effect sample) was used to connect samples to the digital multimeter.

4.1.5 Sample Description

Fig. 4.2 shows the screen with multiple designs used in the ATMA-AT60PD screen printer. The bright regions are the open areas through which the ink passes towards the substrate in the printing process. The designs are metal contacts for solar cells, material test samples and Hall effect samples. The prints obtained from the screen shown in Fig. 4.2 were used subsequently as substrates for the printing of the silicon layers.

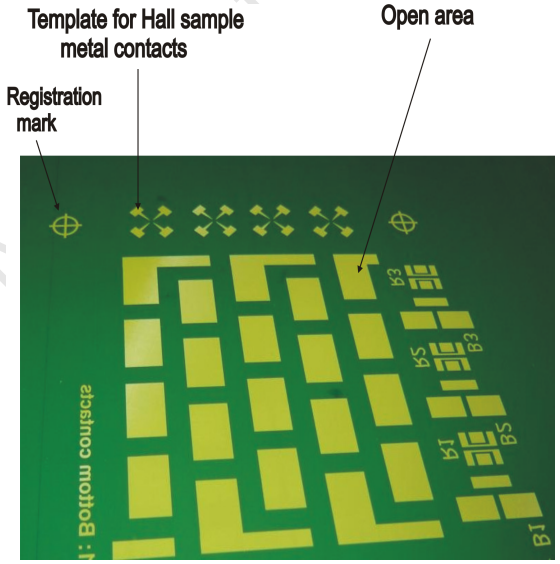

Fig. 4.2: Screen used to print the metal contacts of the Hall samples indicated by the arrow.

Fig.4.3 shows a fully printed sample in van der Pauw geometry. After printing the silver contacts with the screen template shown in Fig.4.2, the silicon layer was printed using a second screen registered to the registration marks shown at the top of Fig. 4.2. The diameter of the printed silicon circle is 2.68mm, and width of the contact at the circumference is 0.45 mm, with a separation of the contacts at about 1.18mm.

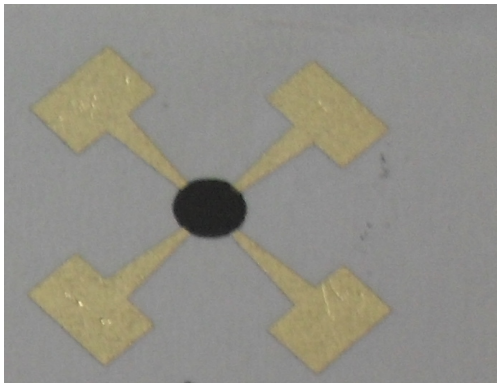

Fig. 4.3: Fully printed Si Hall effect sample in van der Pauw geometry.

The typical thickness of the printed silicon layer was 10 to 20 μm. These dimensions are consistent with the optimal van der Pauw geometry to minimise the error by maintaining the ratio of the contact size to the sample size as approximately $1/6$. Furthermore, the circular structure has been shown to introduce the least error [28, 27], and tapering the contacts along the radius corrects for slight misalignment in the registration of the silicon to the silver layer.

Fig. 4.4 shows one example of a fully printed Hall sample in van der Pauw geometry already mounted on the sample holder. The sample was placed on the sample holder and held in position by the probe tips on a rectangular extension of the silver contact as shown in Figs.4.3 and 4.4. The continuity of the silver contacts to the sample holder was checked using a digital multimeter. Using the meter probes, the resistance was measured between the silver contact and the contact figures Fig. (4.4) on the edge connector of the sample holder for all four connections.

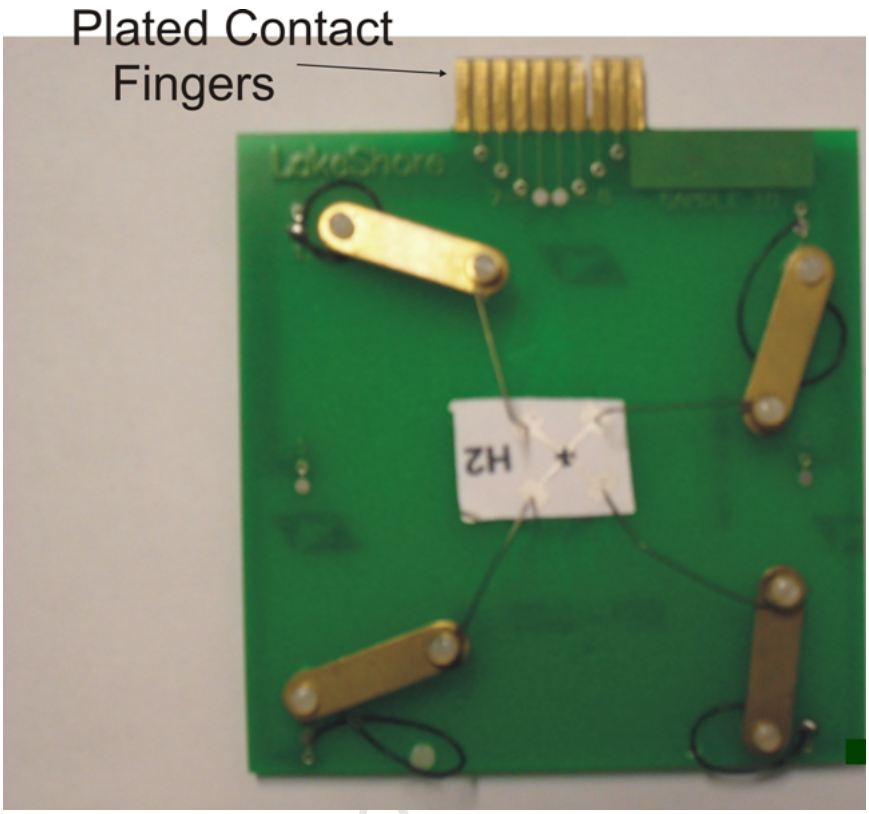

Fig. 4.4: Fully printed sample in van der Pauw geometry mounted on a sample holder ready for Hall effect measurement.

4.2 Experimental Set-Up

4.2.1 Hall Effect Measurement System

The Lake shore Hall effect measurement system (HMS), shown in Fig. 4.5, is designed to measure electronic transport properties of electrically conductive materials. The system consists of two major parts, an electromagnet shown in Fig. 4.6(a), and workstation console system, shown in Fig. 4.6(b).

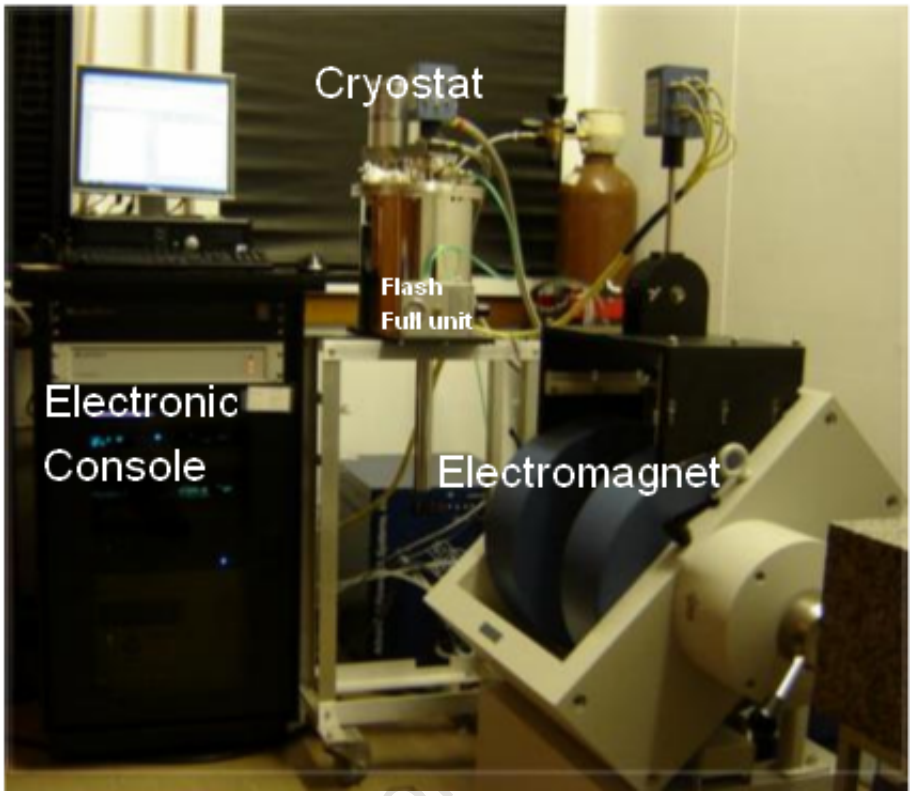

Fig. 4.5: The Lakeshore 7500 Hall effect measurement system.

The electromagnet consists of a magnet stand, magnet pole faces, sample enclosure, and rotating hand knob used to adjust the distance between the pole faces to allow the positioning of either the room temperature sample holder or variable temperature cryostat. For room temperature measurements, the sample is mounted on the sample holder as shown in Fig. 4.4. The sample holder is then inserted into the sample enclosure located on the sample module rod shown in Fig. 4.6(a). The rod is then rotated to place the sample enclosure between the magnetic pole faces and locked into position by the T-lock. The electromagnet is linked to the electronic console via an interface housed in the junction box located at the top of the sample rod.

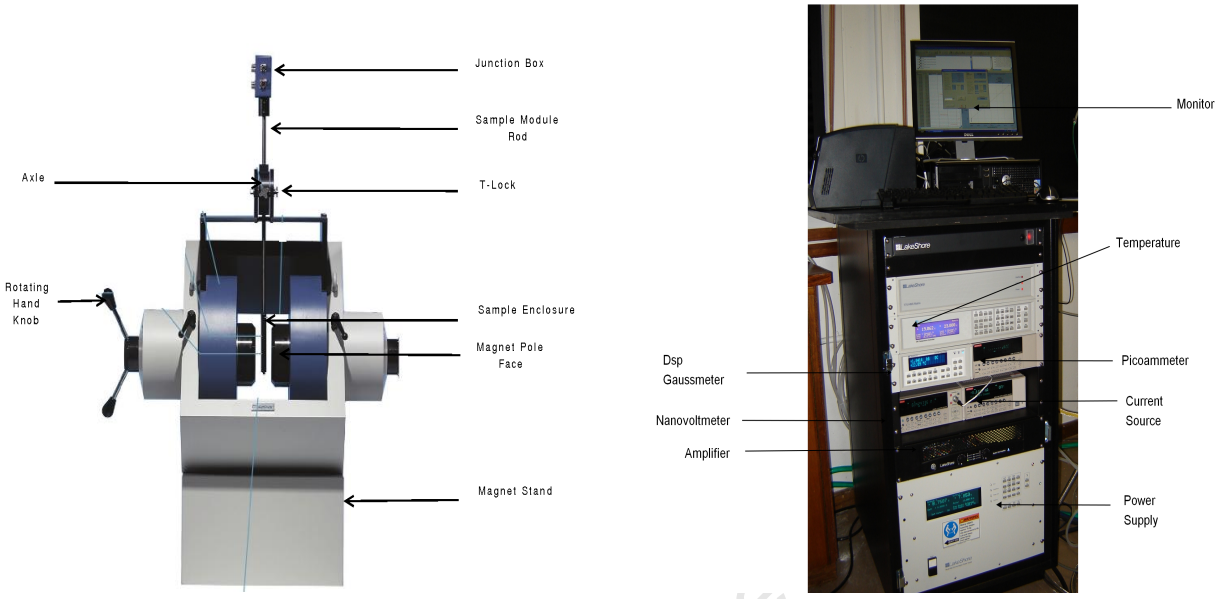

(a) (b)

Fig. 4.6: (a) The electromagnet used for room temperature Hall effect measurement system [44]. (b) Hall effect measurement system workstation console.

Fig.4.5 shows the complete system with the variable temperature cryostat, manufactured by Advanced Research Systems Inc, which is used to perform the variable temperature Hall measurements. The variable temperature system offers a reliable operational range of 150 K - 350 K and enhanced temperature stability conducive for measurement. The sample well in the cryostat is connected to a supply of helium, which acts as the heat exchange gas. A vacuum provides thermal insulation to the sample well in such a way that the only heat exchange that occurs is with the closed cycle refrigerator (CCR) system through a highly conducting metal sheet. Output from the sample and CCR heaters is monitored and controlled by an automatic temperature controller. The sample heater is situated at the bottom of the sample well and the temperature sensor is bonded to the back of the sample card. The CCR temperature sensor and heater are situated at the bottom of the CCR expander. Unlike in the case of the room temperature measurements, where the sample card made use of spring loaded contacts, samples had to be soldered to silver wire, as shown in Fig. 4.7. After soldering the sample, the sample holder insert was then loaded into the well, between the magnetic pole faces, and connected through external electrical cables

to the electronic console. Before any measurement helium gas was then flushed through the sample chamber to exclude atmospheric gases which may condense.

Fig. 4.7: Variable temperature sample holder with mounted sample.

The electronic console is a collection of advanced integrated hardware and control software [27]. The integrated hardware components are: high precision voltmeter (Keithley 2182A Nanovoltmeter), stable current source (Keithley 6220 Precision Current Source), high precision ammeter (Keithley 6485 Picoammeter), electromagnet with Lakeshore 642 Electromagnet Power Supply unit, Lakeshore 475 DSP gaussmeter, HMS Matrix amplifier, Lakeshore 340 temperature controller and sample mounting unit with the heating/cooling mechanism. The Hall system software controls the system instrumentation during an experiment and determines sample resistance, resistivity, Hall coefficient, Hall mobility, carrier concentration, and current voltage characteristics. The software can control and vary current, temperature and magnetic flux density (field) during measurements.

A flow chart, shown in Fig. 4.8, describes the procedures used to measure the current and voltage to calculate the Hall resistance and resistivity of a sample in van der Pauw configuration at both negative and positive fields, as well as the zero field resistivity. Relatively few samples were fully characterised because of the long measurement time as described in the measurement set-up.

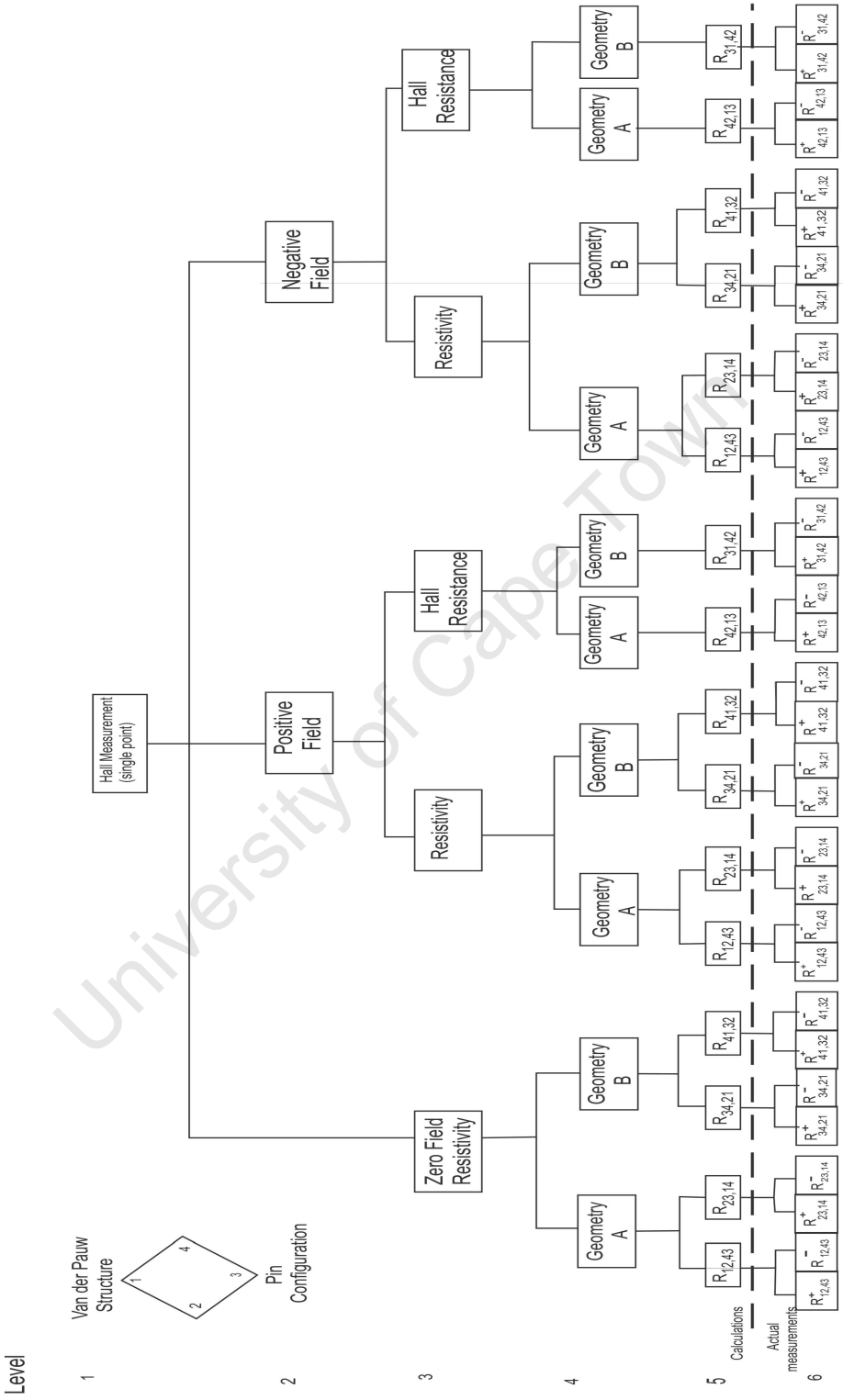

Fig. 4.8: Van der Pauw structure measurement set-up.

4.2.2 IV Measurements

The contact resistances between the sample and Lakeshore sample holder were verified using a Keithley 2000 digital multimeter before loading the sample holder into the sample enclosure, as shown in Fig. 4.6(a). The maximum excitation current for the sample was determined so as to work within the allowed voltage range of $\pm$ 100 V for the Hall measurement system.

Two sample geometries designated A and B, as shown in Fig. 4.9, were used for both IV and variable field measurements. The sample geometries are based on the van der Pauw theory as described in section 3.4.2. IV measurements at zero magnetic field between pairs of contacts were carried out to establish the quality of the contacts. A straight line would indicate ohmic contact behavior which is generally typical of good contacts. In general for the geometry, shown in Fig 4.9, the measurement configurations used were $R_{12,12}$, $R_{23,23}$,$R_{34,34}$ and $R_{41,41}$ as described in chapter 3.

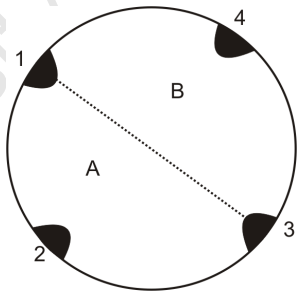

Fig. 4.9: Definition of the geometries for the van der Pauw sample.

Defining the sample geometry is important in order to minimise the errors caused by misalignment of the contacts [27]. The Hall measurement system (HMS) was set up to execute a series of resistance measurements between the opposite contacts on the sample, and also the Hall resistance along the perpendicular direction. The excitation current was applied across one edge, and the potential difference along the opposite edge was measured to calculate the resistance. For example, in Fig. 4.9, when current was applied between points 1 and 2, voltage was measured between points 4 and 3. This gives the resistance $R_{12,34}$ between opposite sides of the sample. The measurements were performed in permutation according to the procedure outlined in the left

branch of the flow chart in Fig.4.8, and the resistance values for two geometries were determined according to equations 3.37 and 3.38.

For geometry A, the resistances $R^{+}_{12,43}$, $R^{-}_{12,43}$, $R^{+}_{23,14}$ and $R^{-}_{23,14}$ are measured. The resistances $R^{+}_{34,21}$, $R^{-}_{34,21}$, $R^{+}_{41,32}$ and $R^{-}_{41,32}$ are measured for geometry B. For example, when the current enters through contact 1 and comes out through contact 2, the potential difference is measured between contact 4 and 3, then the $R^{+}_{12,43}$ is calculated. Likewise, $R^{-}_{12,43}$ is calculated with the reverse current.

4.2.3 Variable Field Measurement

Variable field measurements were obtained for each sample for magnetic field strengths between 1 kG and 10 kG in steps of 1 kG, with a dwell time of 10 s at the same excitation current as the zero field IV curve measurement. Basic parameters such as: the sheet resistivity, Hall coefficient, carrier concentration, Hall voltage and Hall mobility values were calculated using the HMS software. All calculations of sample parameters were based on the van der Pauw theory as described in section 3.4.2. Because the stander software does not provide estimates of uncertainties, these have been calculated from the propagation of the instrumental [44], and geometrical uncertainties [31] as described in Appendix A.

Hall resistance and resistivity are calculated at negative and positive field for both geometries A and B, following the procedure described in the flow chart, Fig. 4.8. The Hall resistance at the positive field is calculated for both geometries according to the central branch of the flow chart. For geometry A, the resistances $R^{+}_{42,13}$ and $R^{-}_{42,13}$are measured. For geometry B, the resistances $R^{+}_{31,42}$ and $R^{-}_{31,42}$ are measured. The same procedure is applied for the negative field shown in the right hand branch of the flow chart. By applying equation (3.46), the Hall coefficient can then be calculated.

To calculate the resistivity for the positive field in both geometries according to the central branch of the flow chart, the resistance $R^{+}_{12,43}$, $R^{-}_{12,43}$, $R^{+}_{23,14}$ and $R^{-}_{23,14}$ are measured for geometry A, and

resistance $R^{+}_{34,21}$, $R^{-}_{34,21}$, $R^{+}_{41,32}$ and $R^{-}_{41,32}$ for geometry B. For example, when the current enters through contact 1 and is out through contact 2, the potential difference is measured between contact 4 and 3, and $R^{+}_{12,43}$ is calculated. Likewise, $R^{-}_{12,43}$ is calculated with the reverse current. The same procedure applies for the negative field shown in the right branch of the flow chart. By applying equation (3.42), the resistivity can then be calculated for dependent field or for zero field.

4.3 Analysis

To analyse the data a general equation combining equations (3.27) and (3.28) was derived to fit the data of the conductivity tensor against field [45]. Origin7 was used to fit the data to this model using a non-linear least square algorithm. From the model function

$$\sigma_{jk} = \frac{e}{2}(1 - erf(B/0.01)) \sum_{i}^{N} \frac{n_i \mu_i^2}{1 + (\mu_i B)^2} + \frac{e}{2}(1 + erf(B/0.01)) \sum_{i}^{N} \frac{n_i \mu_i^2 B}{1 + (\mu_i B)^2} \quad , \tag{4.1}$$

the magnetoconductivity tensor components ($\sigma_{jk} : j, k = x$ or y) could be extracted. The first term on the right hand side of equation 4.1 equals σ_{xx}, and the later term equals σ_{xy}.

The component σ_{xx} is plotted for negative magnetic field (B) while σ_{xy} is plotted for positive magnetic field; e is the electronic charge. The error function (erf) is used to switch between the two individual functions to allow a global fit to both data sets. To avoid an interference with the lowest field measurement, a width of 0.01 T for the error function was used.

Since the sample structure consists of the printed nanoparticulate silicon layer and the paper substrate, the observed variable field properties would be a composition of the two major components. It was therefore imperative to employ a characterisation method using a magnetoconductivity tensor to extract parameters due to the printed silicon as separated from those due to the substrate. The analysis, which was conducted on paper substrate, showed that in dry conditions, it con-

tributes electrons as carriers with sheet carrier density of $(3.66 \times 10^{10} \pm 1.28 \times 10^{9})$ m^{-2} with a mobility of (0.009 ± 0.001) m^2/Vs. This value was taken as a background correction factor for all the subsequent measurement of silicon layers printed on paper substrates. Moreover, the determination of the magnetocounductivity tensor as described in section 3.3 provided a facility for resolving individual carrier mobilities and densities for the complex material, the printed silicon.

5. Results

5.1 Introduction

The field dependent magnetoconductivity measurement or Hall effect measurement is the best characterisation method for materials specifically when more than one carrier type is expected [46]. In this work emphasis is given to silicon in its different forms, such as the original wafers, compressed powder and printed layers. The electrical properties for different particle loading were investigated.

As described in chapter 4, Hall measurements in the van der Pauw geometry were carried out for screen printed samples. For each sample, IV measurements and variable field measurements were used to characterise the material. The various materials characterised included a printed layer containing 88% by weight of particle to binder ratio for *N* and *P* - type silicon, and 80% and 60% *N*-type silicon. The results for all the measurements are presented below.

5.2 N-type Wafer

N-type silicon wafers were supplied by Siltronix AG, Germany. According to the manufacturer's product specification, the wafers were highly doped phosphorous, with a resistivity of $0.01 - 0.05$ Ωcm. The wafers had a thickness of between 475 and 525 μm. The average thickness was measured to be 525 μm for data analysis purposes. A sample with van der Pauw geometry was cut from this wafer with dimensions of approximately 0.6 cm $\times 0.6$ cm . The contacts were ohmic. The bulk resistivity measurement determined with the Hall measurement system yielded a value of $(1.7700 \pm 0.0006) \times 10^{-4}$ Ωm and a sheet resistivity of $(3.380 \pm 0.001) \times 10^{-1}$ Ω/sqr, which confirmed the values stated in the manufacturer's specification.

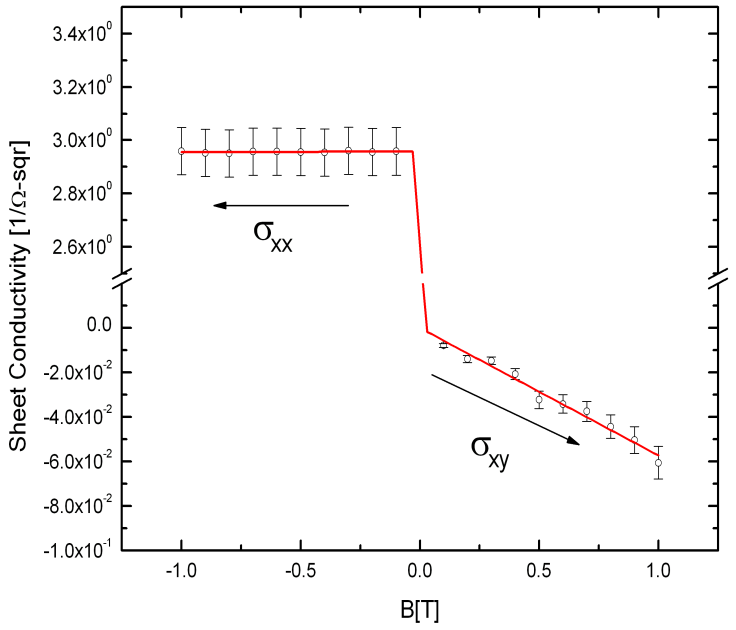

Fig. 5.1: Single carrier fit to the magnetoconductivity tensor for the *N*-type silicon wafer. The solid line is a fit to the model given by equation 4.1.

The data captured using the variable field Hall effect measurement was fitted to the combined conductivity tensor, as shown above in Fig. 5.1. The error bars for σ_{xx} and σ_{xy} were calculated by error propagation using the instrumental accuracy [44] and the uncertainties associated with the sample geometry [31], as described in Appendix A, and the data was fitted with an unweighted least squares fit to equation 4.1. From the fitting, only the presence of a single carrier type could be reliably determined. The carriers were found to be electrons, with sheet density of (9.5 ± 0.2) $\times 10^{20}$ m^{-2}, and mobility of (1.94 ± 0.05) $\times 10^{-2}$ m^2/Vs. The corresponding bulk carrier density is $(1.81 \pm 0.04) \times 10^{24}$ m^{-3}. These results are consistent with the average values obtained from the Hall effect measurement using the standard software provided with the instrument.

5.3 N-type Powder

For Hall effect characterisation, pellets with a diameter of 10 mm and thickness of 1.2 mm were produced by compressing the powder. The dimensions of these samples satisfied the conditions for the van der Pauw geometry, discussed in chapter 3, and the measurement was performed accordingly. The data from the variable field measurement of the sample was fitted to the combined conductivity tensor, with the errors on σ_{xx} and σ_{xy} calculated by error propagation using the instrumental accuracy and the uncertainties associated with the sample geometry [31], as described in Appendix A. Fig. 5.2 shows a constant σ_{xx} with increasing field for the *N*-type powder, indicating a normal magnetoresitivity behaviour. The majority carriers are electrons with a concentration of $(3.4 \pm 0.5) \times 10^{15}\text{m}^{-2}$.

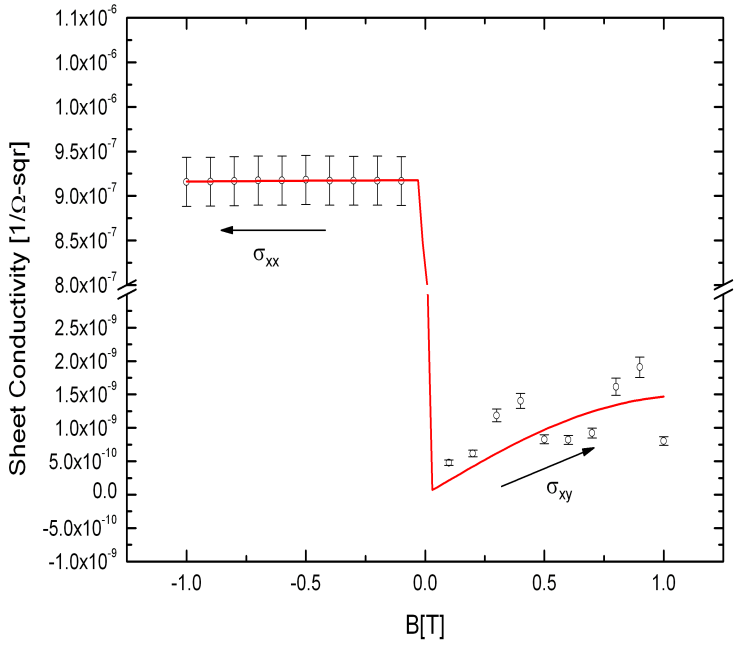

Fig. 5.2: Two carrier fitting to the magnetoconductivity tensor for the *N*-type silicon powder compressed to form a pellet. The solid line is a fit to the model given by equation 4.1.

As a test of consistency both the sheet and bulk conductivities were fitted independently. Within statistical uncertainties, the fitted parameters are consistent for both methods, as seen in table 5.1.

Table 5.1: Summary of the field dependent magnetoconductivity analysis for the *N* type silicon pellet, using both bulk and sheet conductivity values.

Carrier Type	Bulk		Sheet	
	Carrier Concentration[m^{-3}]	Mobility[m^2/Vs]	Carrier Concentration [m^{-2}]	Mobility[m^2/Vs]
Electron	$(2.8 \pm 0.5) \times 10^{18}$	$(1.7 \pm 0.3) \times 10^{-3}$	$(3.4 \pm 0.5) \times 10^{15}$	$(1.7 \pm 0.3) \times 10^{-3}$
Hole	$(8.3 \pm 0.7) \times 10^{13}$	$(4.8 \pm 0.4) \times 10^{-1}$	$(1.0 \pm 0.03) \times 10^{11}$	$(4.7 \pm 0.4) \times 10^{-1}$

5.4 Printed 88% P-type Silicon

Because of the unusual nature of the printed samples, the zero field IV characteristics for all samples measured were determined to establish the quality of the contacts [27, 45]. A good quality contact is one which exhibits ohmic properties at low excitation current. Fig. 5.3, shows an example of a linear fit about the origin of an IV measurement of a printed 88% *P*-type silicon sample. Although there is some deviation at higher excitation current, in the central region the characteristic curve is linear. This range was used to determine the excitation current for the field dependent van der Pauw measurements.

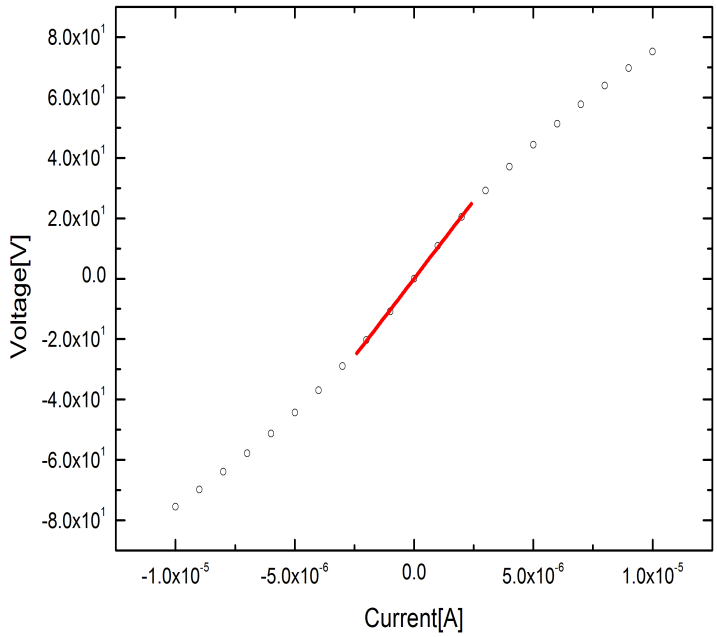

Fig. 5.3: IV-Curve of *P*-type silicon 88% by weight, showing the linear region (straight line) used to determine the resistance. The instrumental uncertainties are smaller than the symbols used.

The carrier type of a material and the concentration of the carrier are determined from the variable field Hall effect measurements using the standard software as described in chapter 3. As an example, Fig. 5.4 shows the sheet Hall coefficient as a function of the applied magnetic field for a printed 88% *P*-type silicon sample. The data in Fig. 5.4 indicate that the majority carriers are holes because most of the data points indicate a positive Hall coefficient. However, the scatter on the data is large compared to the statistical error, calculated from the error propagation of the instrumental accuracy and the geometry error of the van der Pauw arrangement, as described in Appendix A, and the absolute value of the Hall coefficient is low. Negative values are possible within experimental uncertainty, and this simple analysis is inconclusive. Hence a more complete investigation using the behaviour of the magnetoconductivity tensor is necessary.

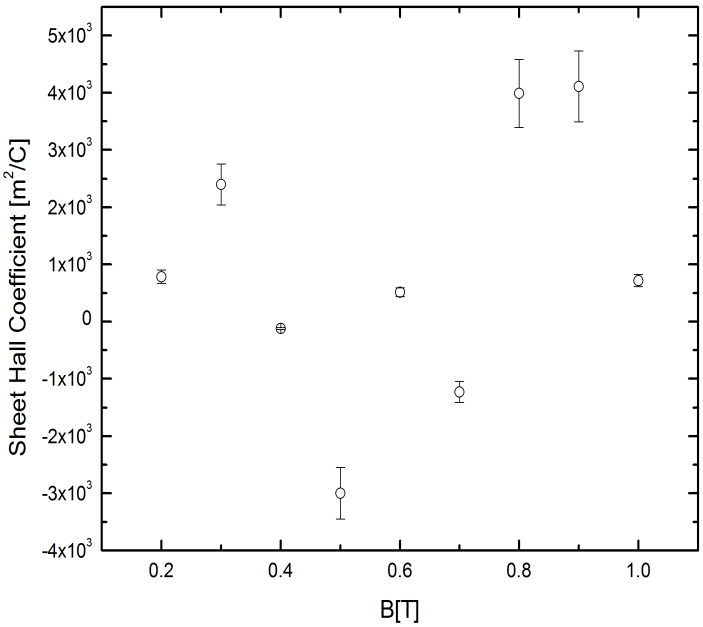

Fig. 5.4: Sheet Hall coefficient versus magnetic field for printed 88% particle loading *P*-type silicon sample, the majority carriers are holes. The error bars shown represent the statistical errors only.

To determine the carrier concentrations and their Hall mobilities, the combined components of the conductivity tensor versus magnetic field were fitted using equation (4.1), as described in section 3.3, using a least squares fit. The presence of at least two carrier types was determined for most of the samples. The sheet conductivities, σ_{xy} and σ_{xx}, were calculated using data extracted from the variable field measurements, and applying this data to equations (3.25) and (3.26). The error bars on σ_{xy} and σ_{xx} were then calculated by error propagation using the instrumental accuracy [44] and the uncertainties associated with the sample geometry [31], as described in Appendix A. To plot both curves on the same axes, the values of σ_{xx} were plotted on the negative axis for the magnetic field. This is illustrated in Fig. 5.5, which shows a fit of the combined conductivity tensor to the data for the printed 88% *P*-type silicon sample.

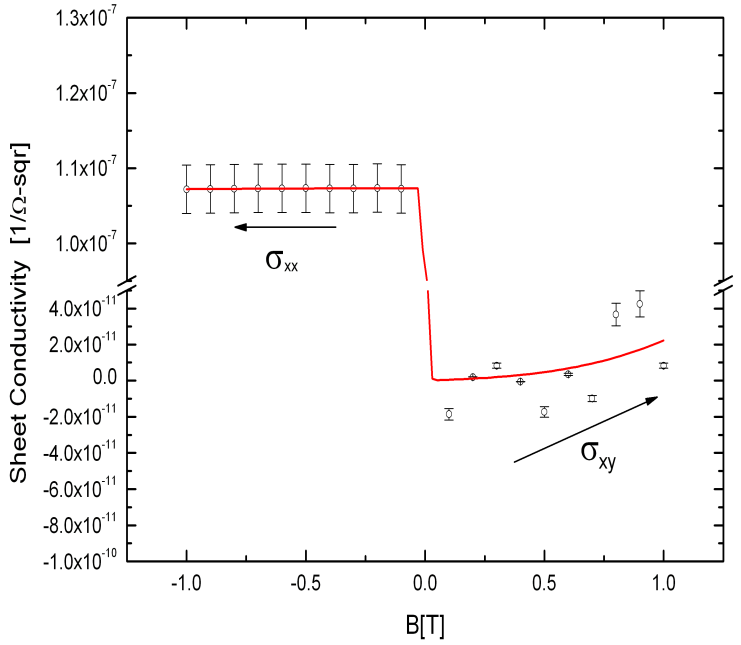

Fig. 5.5: The conductivity tensor versus magnetic field for printed 88% particle loading *p*-type silicon sample. The solid line is a fit to the model given by equation 4.1 with a majority carrier concentration $(9.9 \pm 0.1) \times 10^{13}$ m^{-2}.

Fig. 5.5 above shows a constant σ_{xx} with increasing magnetic field indicating a normal magnetoresistivity behaviour. From the best fit of the data, the majority carriers are holes with a sheet carrier concentration of $(9.9 \pm 0.1) \times 10^{13}$ m^{-2} and a mobility of $(6.5 \pm 0.2 \times) 10^{-3}$ m^2/Vs. The minority carriers are electrons, having a sheet carrier concentration of $(1.5 \pm 0.8) \times 10^{11}$ m^{-2} and a mobility of $(1.6 \pm 0.4) \times 10^{-1}$ m^2/Vs.

Table 5.2 shows a summary of the sheet carrier concentration and mobility for *P*-type materials that were measured. n_1 and μ_1 are respectively the sheet carrier concentration and mobility for majority carriers, while n_2 and μ_2 are the sheet carrier concentration and mobility for minority carriers, which are holes and electrons respectively.

Although the uncertainty in the sheet resistivity is very small, because this is the sum of the product of the carrier concentrations and the mobilities, the errors on these extracted parameters

are large compared to their magnitudes.

Table 5.2: Summary of the result of sheet carrier concentration and mobility for printed 88% *P*-type silicon sample. A negative carrier concentration indicates electrons.

No.	ρ_{sheet} $[\Omega/sqr]$	Majority Carrier		Minority Carrier	
		n_1 [m^{-2}]	μ_1 [m^2/Vs]	n_2[m^{-2}]	μ_2 [m^2/Vs]
1	$1.36\times10^7\pm9\times10^2$	$(6.2\pm0.7)\times10^{14}$	$(7.4\pm0.8)\times10^{-4}$	$(-3.4\pm0.6)\times10^{9}$	$(2.6\pm0.5)\times10^{-1}$
2	$9.32\times10^6\pm1.5\times10^3$	$(9.9\pm0.1)\times10^{13}$	$(6.5\pm0.2)\times10^{-3}$	$(-1.5\pm0.8)\times10^{11}$	$(1.6\pm0.4)\times10^{-1}$

5.5 Printed 88% N-type Silicon

Similar measurements were preformed on printed layers of *N*-type silicon, 88% mixed by weight of particle to binder ratio. Fig. 5.6 shows a similar IV curve for an *N*-type sample, similar to that obtained for the *P*-type layers. The graph shows ohmic behaviour close to the origin, which was the range used to determine the excitation current used for the field dependent measurements.

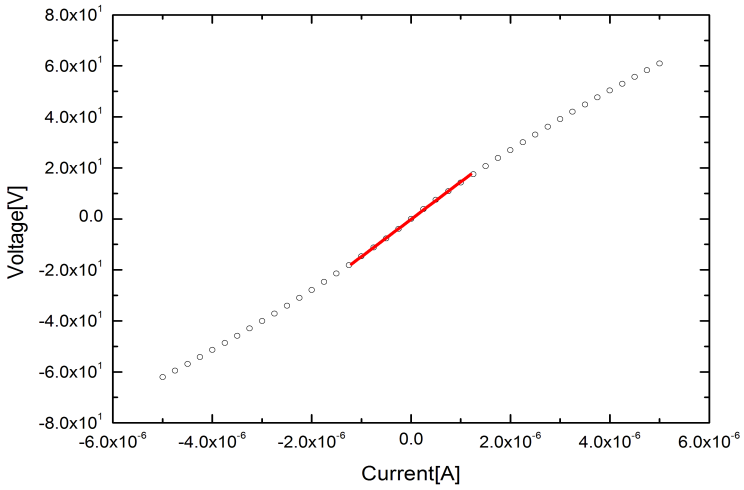

Fig. 5.6: IV-Curve of *N*-type silicon with a particle loading of 88% by weight, showing the linear region used to determine resistance. The instrumental uncertainties are smaller than the symbols used.

Fig. 5.7 shows the sheet Hall coefficient versus applied magnetic field for a printed 88% *N*-type silicon sample. The majority carriers are most likely electrons because most of the data points have negative values, thus indicating a negative Hall coefficient. As for the *P*-type materials, the scatter on the data make this simple analysis inconclusive, and further investigation of the magnetoconductivity tensor is necessary.

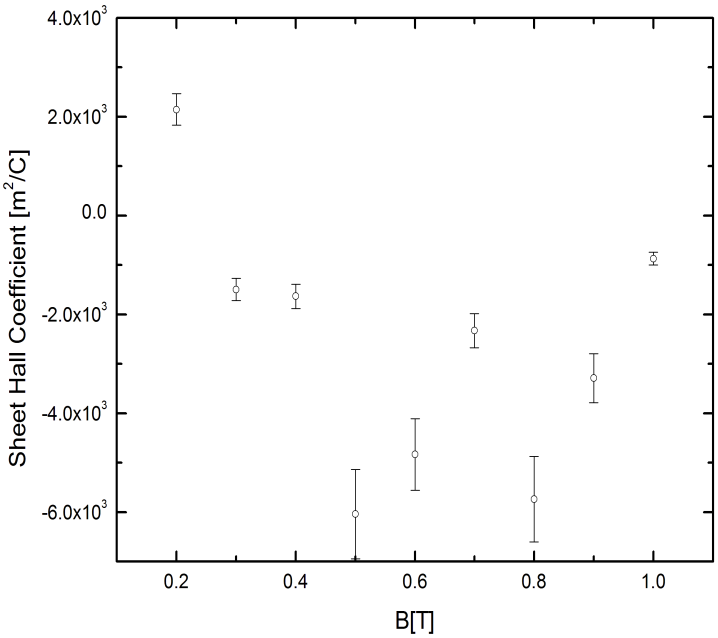

Fig. 5.7: Sheet Hall coefficient versus magnetic field for printed 88% particle loading *N*-type silicon sample. The error bars shown are the statistical error only.

Fig. 5.8 shows constant σ_{xx} with increasing field for the printed 88% *N*-type silicon sample indicating a normal magnetoresitivity behaviour. From the best fit of the data the majority carriers were electrons with sheet carrier concentration $(1.6 \pm 0.5) \times 10^{14}$ m^{-2} and the mobility $(3.3 \pm 1.0) \times 10^{-3}$ m^2/Vs. The minority carriers were holes, with a sheet carrier concentration of $(4.4 \pm 3.3) \times 10^{9}$ m^{-2}, and the mobility of $(7.5 \pm 2.3) \times 10^{-1}$ m^2/Vs.

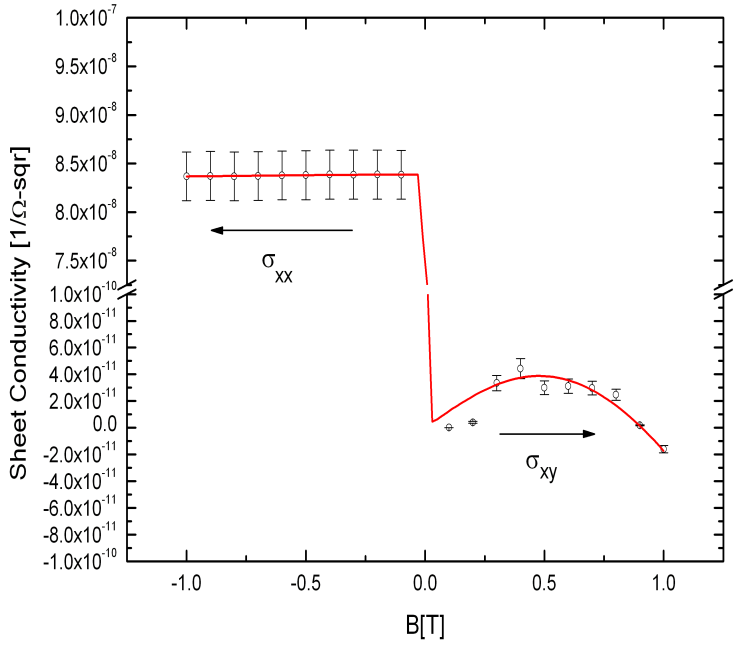

Fig. 5.8: The conductivity tensor versus field, for the printed 88% particle loading *N*-type sample. The majority carriers are electrons with a concentration of $(1.6 \pm 0.5) \times 10^{14}$ m^{-2}.

Table 5.3 shows a summary for the different printed 88% *N*-type silicon samples. n_1 and μ_1 are, respectively, the sheet carrier concentration and mobility for the majority carriers which are electrons, while n_2 and μ_2 are the sheet carrier concentration and mobility for the minority carriers which are holes.

As in table 5.3, correlation between the extracted concentrations and mobilities leads to large uncertainties compared to the uncertainty in the sheet resistivity.

Table 5.3: Summary of the carrier concentration and mobility for the 88% particle loading *N*-type silicon printed sample. A negative concentration indicates eletrons.

No.	ρ_{sheet} [Ω/sqr]	Majority Carrier		Minority Carrier	
		n_1 [m^{-2}]	μ_1 [m^2/Vs]	n_2 [m^{-2}]	μ_2 [m^2/Vs]
1	$1.19\times10^7\pm3\times10^3$	$(-1.6\ \pm\ 0.5)\ \times10^{14}$	$(3.3\pm1.0)\times10^{-3}$	$(4.4\pm3.3)\times10^9$	$(7.5\pm2.3)\times10^{-1}$
2	$3.13\times10^7\pm1\times10^4$	$(-5.590\ \pm\ 0.006)\times10^{13}$	$(3.5300\ \pm\ 0.0003)\times10^{-3}$	$(3.1\pm0.7)\times10^9$	$(6.1\pm0.8)\times10^{-1}$
3	$5.57\times10^6\pm3\times10^4$	$(-1.79\pm0.04)\times10^{13}$	$(4.4200\ \pm\ 0.0006)\times10^{-2}$	$(3.0\pm0.4)\times10^{12}$	$(1.08\ \pm\ 0.07)\ \times10^{-1}$

5.6 Effect of Particle Loading on Carrier Concentration

To determine the effect of particle loading on the carrier properties, similar measurements and analysis were carried out for layers of *N*-type silicon material containing 80% and 60% by weight of particle to binder ratio printed on paper substrates. Figures 5.9(a) and 5.9(b) show a combined graph of average sheet resistivity and carrier concentration respectively, for the average value of printed 60%, 80% and 88% *N*-type silicon samples.

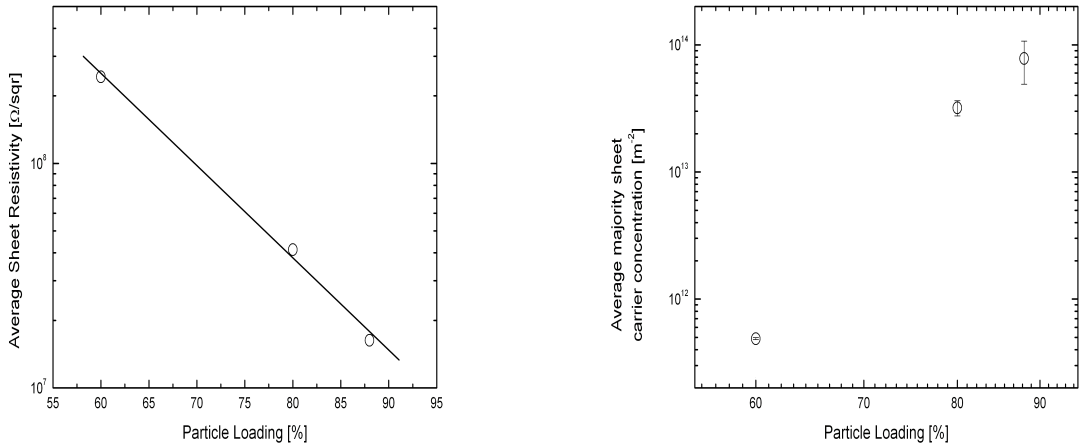

(a) (b)

Fig. 5.9: (a) Average sheet resistivity as a function of the particle loading for *N*-type silicon printed samples. The solid line is guide to the eye. (b) Average sheet carrier concentration. Where no error bars are shown the statistical errors are smaller than the size of the symbols used.

Fig.5.9(a) shows an approximately exponential decrease in sheet resistivity with the particle loading. Fig.5.9(b) shows that the majority carrier density has a complementary approximate exponential increase with particle loading. The reason for this is not clear yet, but is related to the structure and the peaking of particles in the layer. The Hall mobility remains approximately constant with particle loading at $(1.24 \pm 0.03) \times 10^{-2}$ m^2/Vs. This is to be expected because the Hall mobility is a local property related to the individual particle size and the structure of the interface between particles, and not the number of connections.

5.7 Effect of Temperature on The Hall Effect in Printed Silicon

The effect of temperature on the carrier concentration and mobility of the material was investigated above room temperature using the Hall measurement system (HMS). The temperature was taken from $290 - 325$ K, with 325K being the highest temperature safely attainable. Fits of

the components of the combined conductivity tensor for various temperature measurements of printed *N*-type silicon are shown in Fig. 5.10. All the fits indicate that electrons are the majority carriers, except at T=295 K, shown in Fig. 5.10(b), where the analysis shows a mixed carrier type with holes appearing to dominate. The reason for this is not clear, but the total carrier concentration determined is low compared to the other measurements.

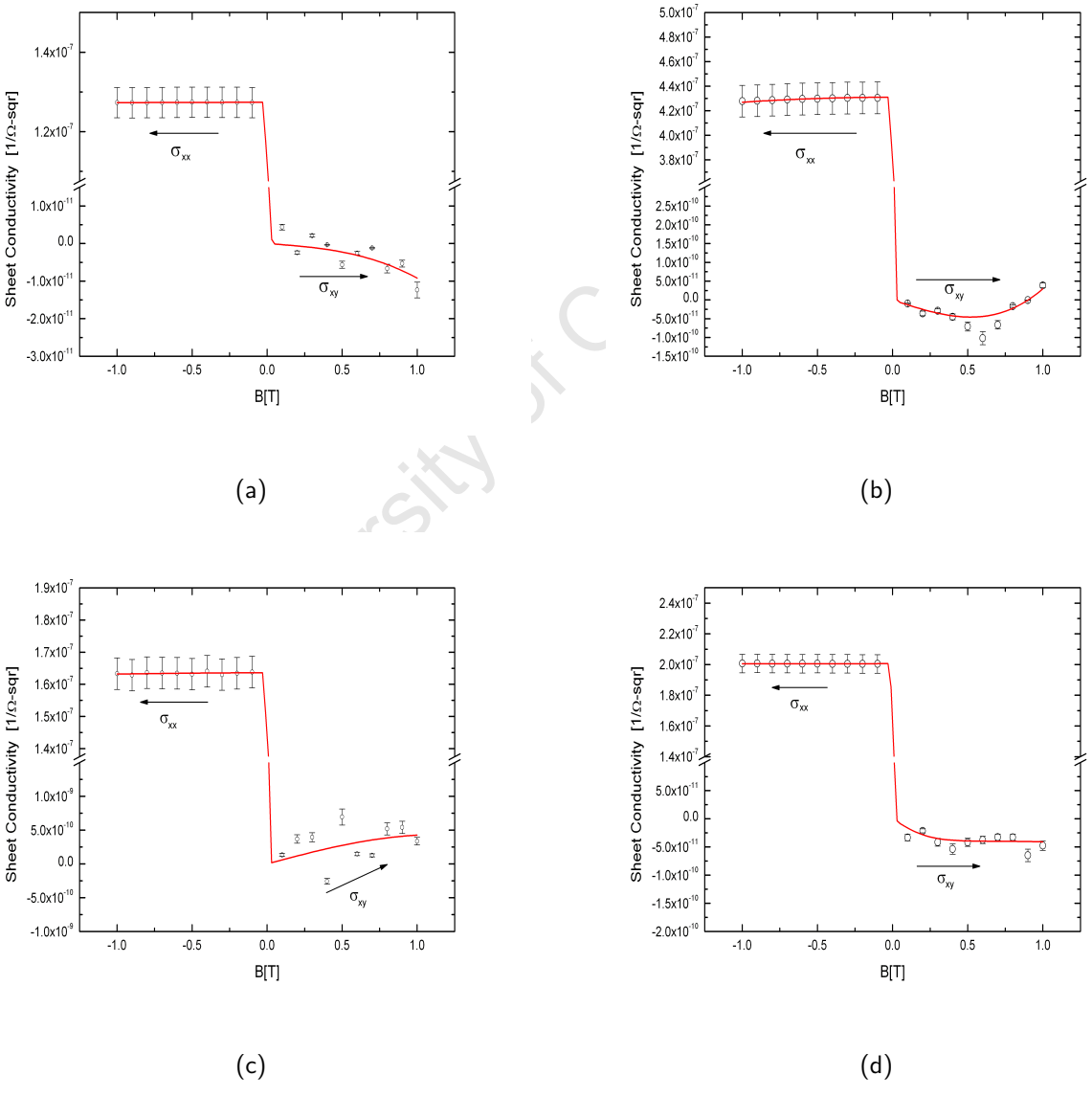

Fig. 5.10: Temperature dependence of the conductivity tensor components in printed *N*-type silicon, (a) T=290 K, (b) T =295K, (c) T =315K and (d) T =325K.

Table 5.4: Summary of the result for effect of temperature on carrier concentration for printed *N*-type silicon.

Temperature[K]	Majority Carrier		Minority Carrier	
	$n_1[\ m^{-2}]$	$\mu_1\ [m^2/Vs]$	$n_2[\ m^{-2}]$	$\mu_2\ [m^2/Vs]$
T=290	$(-7.6 \pm 0.2) \times 10^{13}$	$(9.3 \pm 4.3) \times 10^{-3}$	$(1.1 \pm 0.4) \times 10^{12}$	$(7.8 \pm 2.3) \times 10^{-2}$
T=295	$(2.0 \pm 0.1) \times 10^{13}$	$(8.0 \pm 0.1) \times 10^{-2}$	$(-9.0 \pm 0.3) \times 10^{12}$	$(1.20 \pm 0.02) \times 10^{-1}$
T=315	$(-3.240 \pm 0.002) \times 10^{14}$	$(3.110 \pm 0.002) \times 10^{-3}$	$(3.8 \pm 0.6) \times 10^{10}$	$(4.3 \pm 0.7) \times 10^{-1}$
T=325	$(-1.3 \pm 0.4) \times 10^{16}$	$(9.95 \pm 0.09) \times 10^{-5}$	$(-1.5 \pm 0.2) \times 10^{8}$	$(2.5 \pm 0.1) \times 10^{0}$

Table 5.4 above shows a summary of the effect of temperature on the carrier concentration and mobility. n_1 and μ_1 are the sheet carrier concentration and mobility, respectively, for majority carriers, which are electrons, and n_2 and μ_2 are sheet carrier concentration and mobility, respectively, for the minority carrier holes.

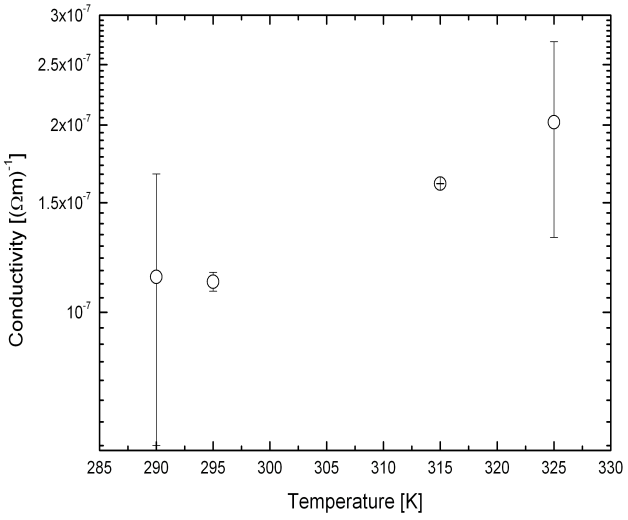

Fig. 5.11: Temperature dependence of the majority carrier conductivity of printed *N*-type silicon.

From table 5.4 the contribution of the majority carriers (electrons) to the conductivity could be determined. Fig. 5.11 above shows the effect of variable temperature on the electron contribution to the conductivity for the printed *N*-type silicon Hall sample. Taking the large uncertainty at 290K, the data suggest a thermally activated charge transport process.

6. Discussion

Variable field measurements of the Hall coefficient for printed silicon nanoparticle layers indicate the presence of two carrier types in all samples. For the printed *P*-type silicon, the expected majority carriers are holes. Similarly, for the *N*-type printed silicon the majority carriers are electrons. However, in both cases the scatter on the data does not allow further conclusions to be drawn using this simple analysis.

Results from the fit of the components of the conductivity tensor (equation 4.1) also indicate the presence of two carrier types, as shown in tables 5.2 and 5.3. The average sheet carrier concentrations at room temperature determined for the printed 88% *P*-type silicon sample were $(3.60 \pm 0.49)\ \times 10^{14}$ m^{-2} for the majority carriers, which are holes, and $(7.7 \pm 5.7)\ \times 10^{10}$ m^{-2} for the minority carriers, which are electrons. On the other hand, the average mobility for the majority carriers was lower than that of the minority carriers as indicated in table 5.2. This is expected from the conductivity equation (2.14). Since at ambient temperature, only the majority carriers need to be considered [47], the conductivity of the printed 88% *P*-type silicon, excluding the substrate, was calculated to be $(2.08 \pm 0.32) \times 10^{-7}\ \Omega^{-1}\cdot$ m^{-1}, and for the printed 88% *N*-type silicon it was calculated to be $(2.13 \pm 0.79) \times 10^{-7}\ \Omega^{-1}\cdot$ m^{-1}. The conductivities are representative of the expected majority carrier types and concentrations.

The printed 88% and 80% *N*-type silicon samples have carrier concentrations in the same order of magnitude. This seems to suggest that there could be a percolation threshold where the effective carrier concentration no longer changes with increase in particle loading. Also, in the layers printed with 60% particle loading, the carrier concentration is 2 orders of magnitude lower than the others. This is an expected result, which gives credibility to both the method of measurement and the analysis. However, extensive measurements using a larger set of different particle loadings would be useful to investigatate the presence of a percolation threshold.

From the Hall effect measurements of the different forms of the silicon material, the variation of

the carrier concentration was obtained. The principal material, which was the *N*-type silicon wafer used to produce the nanoparticles, showed carrier concentrations and mobilities in agreement with the manufacture's specification. This was used to confirm the credibility of both measurement and analysis methods. Comparing the results from the wafer, pellets and printed samples, the carrier concentration and conductivity dropped significantly because there is constricted current path, since the layer is formed through a network of individual silicon particles. The drop in the carrier concentration in the pellet compared to the bulk silicon wafer can be explained in terms of lower densities of the pellet due to the open structure, resulting from spaces between particles. In the printed layers, the nanoparticulate silicon network is permeated by the insulating binder, which creates spatially distributed conducting patches, which further reduces the effective carrier density. On the other hand,the Hall mobility has shown a relative constancy in the three tested types of materials: bulk, compressed powder, and printed layers.

It was observed that the conductivity increases with increasing temperature (Fig. 5.11). This is further evidenced from Table 5.4, where increase in temperature corresponds to increasing carrier concentration, and thus increasing conductivity. The conductivity can thus be said to be thermally activated. In addition, it has been observed that there is no well defined relationship between the Hall mobility and the temperature. This observation is consistent with a hopping transport mechanism between small particles or grains, where the thermal activation of the conduction is expected to be seen in the carrier concentration and not the mobility [48]. The particles used in this work have median sizes of approximately 80 nm, with grain sizes around $10 - 15$ nm [39].

However, more work needs to be carried out to investigate the transport mechanism, in particular whether it is single range hopping between individual particles or grains, or variable range hopping within clusters of particles. Also, a more detailed temperature analysis will yield valuable information on the barrier and possible trapped states. This will help to fully characterise the electrical properties of the printed materials, which have been shown to work in electronic devices [49].

7. Conclusion

The main objective of this work was to study the electrical properties of screen printed nanoparticulate silicon using a Hall measurement system employing a four point system, based on the van der Pauw geometry. A combined model to simultaneously analyse the transverse and longitudinal components of magnetoconductivity tensor, was developed and successfully applied to the printed silicon material to extract important electrical parameters of the materials. For purposes of comparison, the model was also applied to doped bulk silicon and compressed pellets of silicon powder.

The carrier concentration decreased during milling of the silicon and also during preparation of printed silicon layers. Hall mobilities were determined to be of the same order of magnitude for the three forms of silicon studied. The three forms of silicon showed two carrier types as determined from the magnetoconductivity tensor components of the model. Mobility values for the printed silicon layers were comparable to those of amorphous silicon and organic semiconductors.

For the printed silicon layers, it was established that sheet resistivity decreased with increasing particle loading. Carrier concentration increased with an increase in particle loading up to a percolation threshold, and shows indication of saturation beyond this percolation threshold. Particle loading was therefore established to be an important parameter that can be employed to tune the electrical properties of printed silicon, such as sheet resistivity and carrier concentration.

For the same particle loading, variable temperature Hall measurements showed that the effective carrier concentration increased with increasing temperatures between 290 K and 325 K, whereas no clear trend was observed for the mobility. This demonstrates that the printed nanoparticlulate silicon is a strong candidate for making temperature sensitive devices, such as thermistors. With further investigations into the thermal response of the printed silicon, it should be possible to decipher information concerning charge transport in the material.

Appendix A. Error Analysis

This section deals with methods used to determine the uncertainties in the components of the conductivity tensors σ_{xx} and σ_{xy}. It is important to mention that the Hall measurement system (HMS) software does not give any error estimates for any measured or estimated parameters. Thus there is a need to use error propagation, taking into account the instrumental accuracy and error in sample geometry, as explained below. Other unknown quantities, such as the Hall factors (chapter 3) for these materials, or systematic errors, such as the instrumental alignment, are not taken into account.

- Instrumental Accuracy: given as $\frac{\Delta\rho}{\rho} = 2\%$ and $\frac{\Delta R_H}{R_H} = 5\%$ [44], where ρ and R_H are the resistivity and Hall coefficent, respectively.

- Geometry Errors

  The uncertainty in the resistivity and Hall coefficient due to the sample geometry are obtained as [31],

$$\begin{aligned} \frac{\Delta\rho}{\rho} &= \frac{d_1^2}{16D^2\ln 2} + \frac{d_2^2}{4D^2\ln 2} \quad , \\ \frac{\Delta R_H}{R_H} &= \frac{2d_1}{\pi^2 D} + \frac{4d_2}{\pi^2 D} \end{aligned} \tag{A.1}$$

  where D is the diameter of the sample, and d_1 and d_2 are the dimensions of the contacts as shown in Fig. A.1.

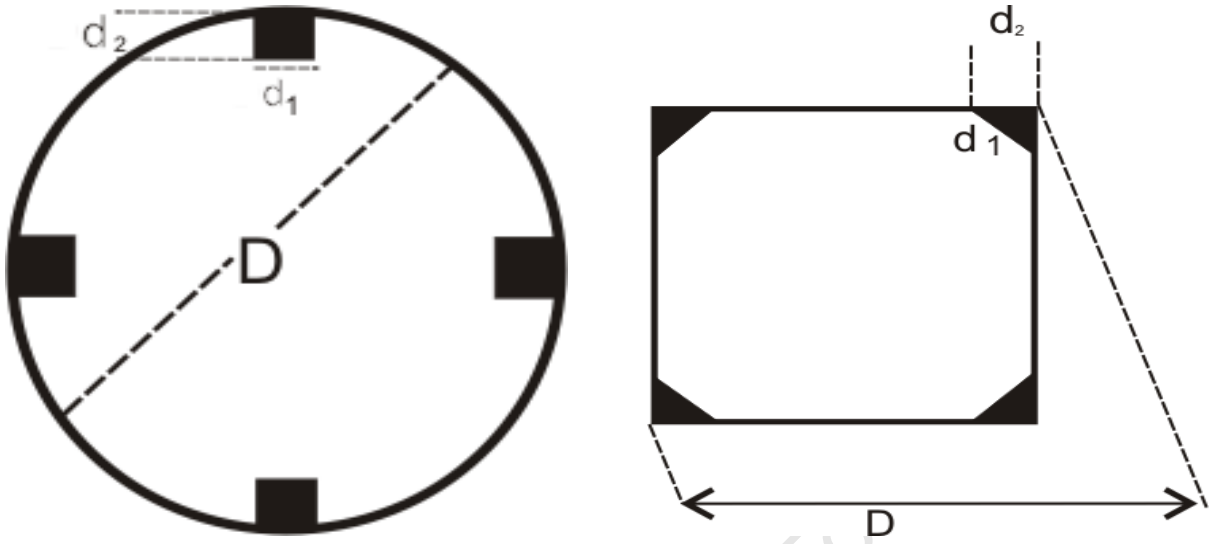

(a) (b)

Fig. A.1: The geometrical dimension for (a) round and (b) square samples.

From equations A.1, the geometry error is determined to be $\frac{\Delta\rho}{\rho} = 1\%$ and $\frac{\Delta R_H}{R_H} = 15\%$ for the printed samples; $\frac{\Delta\rho}{\rho} = 1\%$ and $\frac{\Delta R_H}{R_H} = 10\%$ for the square wafer geometry, and $\frac{\Delta\rho}{\rho} = 1\%$ and $\frac{\Delta R_H}{R_H} = 6\%$ for a compressed powder pellet.

The conductivity along the current direction σ_{xx} as given in equation (3.25) is,

$$\sigma_{xx} = \frac{\rho_{xx}}{\rho_{xx}^2 + (R_H B)^2} \quad . \tag{A.2}$$

Now, set

$$\begin{aligned} \rho &= \rho_{xx} \quad , \\ R &= R_H B \quad , \\ D &= \rho_{xx}^2 + (R_H B)^2 \quad . \end{aligned} \tag{A.3}$$

Then, equation (3.25) yields

$$\sigma_{xx} = \frac{\rho}{D} \quad . \tag{A.4}$$

To find the error in measuring the conductivity, partially differentiate the equation above once with respect to ρ and then to R. Take the absolute value,

$$\begin{aligned} \left|\frac{\partial \sigma_{xx}}{\partial \rho}\right| &= \frac{1}{D} + \left| \left(\frac{\partial \sigma_{xx}}{\partial D} \cdot \frac{\partial D}{\partial \rho} \right) \right| \\ &= \frac{1}{D} + \frac{2\rho^2}{D^2} \quad , \end{aligned} \tag{A.5}$$

and

$$\begin{aligned} \left|\frac{\partial \sigma_{xx}}{\partial R}\right| &= \left|\frac{\partial \sigma_{xx}}{\partial R} \cdot \frac{\partial D}{\partial R}\right|, \\ &= \frac{2\rho R}{D^2} \quad . \end{aligned} \tag{A.6}$$

Combining both equations in one, the total error $\Delta\sigma_{xx}$ in determining the longitudinal conductivity σ_{xx} reads

$$\Delta\sigma_{xx} \;=\; \Delta\rho \left(\frac{1}{D} + \frac{2\rho^2}{D^2} \right) + \Delta R \left(\frac{2\rho R}{D^2} \right) \quad . \tag{A.7}$$

In a direction perpendicular to the current flow, equation (3.26) which governs the conductivity in that direction is

$$\sigma_{xy} \;=\; \frac{R_H B}{\rho_{xx}^2 + (R_H B)^2} \quad . \tag{A.8}$$

Again using the values set above for each of ρ_{xx}, $R_H B$, and $\rho_{xx}^2 + (R_H B)^2$, and following the same steps used to calculate $\Delta\sigma_{xx}$, we get

$$\sigma_{xy} \;=\; \frac{R}{D} \quad . \tag{A.9}$$

$$\begin{aligned} \left|\frac{\partial \sigma_{xy}}{\partial \rho}\right| &= \left|\frac{\partial \sigma_{xy}}{\partial D} \cdot \frac{\partial D}{\partial \rho}\right| \\ &= \frac{2\rho R}{D^2} \quad , \end{aligned} \tag{A.10}$$

and

$$\begin{aligned} \left|\frac{\partial \sigma_{xy}}{\partial R}\right| &= \frac{1}{D}\left|\frac{\partial \sigma_{xy}}{\partial D} \cdot \frac{\partial D}{\partial R}\right| \\ &= \frac{2R^2}{D^2} \quad , \end{aligned} \tag{A.11}$$

then, the total error $\Delta\sigma_{xy}$ in the transverse conductivity σ_{xy} is

$$\Delta\sigma_{xy} = \Delta\rho\left(\frac{2\rho R}{D^2}\right) + \Delta R\left(\frac{1}{D} + \frac{2R^2}{D^2}\right) \quad . \tag{A.12}$$

Acknowledgements

Thanks and Praise be to the almighty ALLAH for Grace and Mercy showered upon me to get to the end of the tunnel through my education carrier. I would like to thank the many individuals who have helped me a long on this journey, making each step a little easier than the one before. My supervisors, professors M. Härting and D.T. Britton, for their tremendous support, help and nice guidance. My appreciation also goes to the African Institute for Mathematical Sciences (AIMS), and Department of Science and Technology, through its business unit, the Inovation Fund for their financial support.

To the members of the University of Cape town solid state and Material Physics group, who helped me preparing the samples and understanding the work. Dr.Goro Gonfa was helpful in the how I used the instrument for the measurement and answering my questions. Without his help I could not have done this work. Batsirai Magunje was helpful in preparing the samples, explaining the issues of the material and proofreading my work. Emmanuel Jonah, thank you for being a great friend, helping me in curve fitting, solving latex problem and walking home together at the end of the day. Also thanks to Dr.Shadrack Nsengiyumva, Dr. Raji Abduralfiu, Oluwole Solana, David Unuigbe, Stanley Walton, Stephen Jones and Ntombi Mathe.

I am indebted to my Grandmother, my parents, and my happy family for encouraging me through the difficult times and providing me with warmth and infinite love. There are many Thank to all my friends in University of Khartoum Department of Physics for giving me the necessary encouragement and social support. All my best wish to Buthaina Adam, Maye Elmardi, Maisson Hassan, Mazin Sirry and Mohamed Yaguob for the special time we have spent together.

References

[1] M. Faraday. *Experimental Researches in Electricity*, volume **1**. p.p. 122-124. Richard and John Edward Taylor, London, 1839.

[2] T. H. Grahn. *Introduction to Semiconductor Physics*. World Scientific, Singapore , 1999.

[3] B. Sapoval and C. Hermann. *Physics of Semiconductor*. Springer-Verlag, New York, 1995.

[4] C. C. Koch. Top-Down Synthesis of Nanostructured Materials: Mechanical and Thermal Processing Methods. *Reviews on Advanced Materials Science*, **5**:91–99, 2003.

[5] H. S. Nalwa. *Handbook of Nanostructured Materials and nanotechnology*, volume **3**, Electrical Properties. Academic Press,San Diego, 2000.

[6] C. Suryanarayana and C. C. Koch. Nanocrystalline Materials-Current Research and Future Directions. *Hyperfine Interactions*, **130**:5 – 44, 2000.

[7] D. T. Britton and M. Härting. Printed Nanoparticulate Composites for Silicon Thick Film Electronics. *Pure and Applied Chemistry*, **78**:1723 – 1739, 2006.

[8] K. Seeger. *Semiconductor Physics-An Introduction*. 6th edition, Springer Series, Berlin, 1997.

[9] A. Goetzberger, J. Knobloch, and B. Voss. *Crystalline Silicon Solar Cells*. Wiley, Chichester , 1998.

[10] L. Solymar and D. Walsh. *Electrical Properties of Materials*. Oxford University Press, Oxford, 1998.

[11] E. J. Cassignol. *Semiconductors: Physics and Electronics*, volume **1**. Philips Technical Library, New York, 1966.

[12] D. A. Neamen. *Semiconductor Physics And Devices Basic Principle*. 3rd edition, McGraw-Hill Companices, Inc, New York , 2003.

[13] G. L Pearson and J. Bardeen. Electrical Properties of pure Silicon and Silicon Alloys Containing boron and Phosphorus. *Physical Review*, **75**:865–883, 1949.

[14] H. P. Myers. *Introductory Solid State Physics*. 2nd edition, Taylor & Francis Ltd, London, 1997.

[15] S. M. Sze and K. K. Ng. *Physics of Semiconductor Devices*. 3rd edition, John Wiley and Sons Inc, Hoboken, New Jersey, 2007.

[16] S. P. Parker. *Solid-State Physics Source Book*. Mc Graw-Hill,Inc, New York , 1988.

[17] M. A. Omer. *Elementary Solid State Physics*. Addison Wesly, London, 1975.

[18] C. Kittel. *Introduction to Solid State Physics*. 8th edition,John Wiley, New York , 2005.

[19] L. Solymar and D. Walsh. *Lectures on the Electrical Properties of Materials*. 2nd edition, Oxford University Press, Oxford, 1970.

[20] W. R. Thurber. *Hall Effect Measurements*. http://www.nist.gov/eeel/semiconductor/hall.cfm, National Institute Of Standards and Technology NIST, accessed on 04 August 2010.

[21] H. Ibach and H. Luth. *Solid state Physics An Introduction to Principles of Materials Science*. 2nd edition, Springer, Berlin, 1995.

[22] W.A. Beck and J.R. Anderson. Determination of Electrical Transport Properties Using a Novel Magnetic Field Dependent Hall Technique. *Journal of Applied Physics*, **62**:541–554, 1987.

[23] D. L. Leslie-Pelecky, D. G. Seiler, and M. R. Loloee. New Method of Characterizing Majority and Minority Carriers in Semiconductors. *Applied Physics Letters*, **51**:1916–1920, 1987.

[24] J. Lindemuth, B. Dodrill, J. Meyer, and I. Vurgaftman. Extraction of Low Mobility, Low Conductivity Carriers from Field Dependent Hall Data. *Extended Abstract of Paper Presented at Cs-Max, San Jose, CA, IOP Published Ltd*, pages 48–50, 2002.

[25] J. R. Meyer, C. A. Hoffman, F. J. Bartoli, D. A. Arnold, S. Sivananthan, and J. P. Faurie. Methods for Magnetotransport Characterization of IR Detector Materials. *Semicond. Sci. Technol*, **8**:805–823, 1993.

[26] G. Du, J. R. Lindemuth, B. C. Dodrill, R. Sandhu, M. Wojtowicz, M. S. Goosky, I. Vurgaftman, and J. R. Meyer. Characterizing Multi-Carrier Devices with Quantitative Mobility Spectrum Analysis and Variable Field Hall Measurements. *http://www.lakeshore.com/pdf_files/systems/Hall_Data_Sheets/IPRM%20Paper.pdf*, accessed on 02 April 2009.

[27] Lake Shore Cryotronics, Inc. *Lake Shore 7500/9500 Series Hall System Users Manual*. Available at: `http://www.lakeshore.com/pdf file, accessed on 15 August 2008.`

[28] D. C. Look. *Electrical Characterization Of GaAs Materials and Devices*. John Willy and Sons, Chichester, 1989.

[29] D. K. Schroder. *Semiconductor Material and Device Characterization*. 3rd edition, John Wiley and Sons, Chichester, 2006.

[30] C.K. Sumesh, K.D. Patel, V.M. Pathak, and R. Srivastava. An Insight to Improved Van der Pauw Factor and Their Stability in The Temperature Rang 300K-10K of Layered Semiconducting Material, Molybdenum Diselenide Single Crystals. *Journal of Applied Crystallography*, **5**:303–308, 2008.

[31] L. J. Van der Pauw. A Method of Measuring Specific Resistivity and Hall Effect of Discs of Arbitrary Shape. *Philips Research Reports* , **13**:1–9, 1958.

[32] A. P. van Gelder. A New Method for Measuring the Conductivity of Arbitrary Shaped two-dimensional Sample. *Physical B*, **204**:149–152, 1995.

[33] L. J. van der Pauw. A Method of Measuring Specific Resistivity and Hall Coefficient on Lamellae of Arbitrary Shape. *Philips Technical Review*, **20**:220–224, 1958.

[34] Y. Sun, J. Shi, and Q. Meng. Measurement of Sheet Resistance of Cross Microareas Using a Modified Van der Pauw Method. *Semiconductor Science and Technology*, **11**:805–811, 1996.

[35] A. S. Edelstein, R. C. Cammarata, and A. E. Edelstein. *Nanomaterials: Synthesis, Properties and Applications*. Taylor & Francis Group, New York, 1996.

[36] O. D. Solana. *Production and Characterisation of Nanoparticulate Silicon Photovoltaic Devices*. Msc Thesis, University of Cape Town, 2009.

[37] C. L. De Castro and B. S. Mitchell. Nanoparticles from Mechanical Attrition. *American Scientific Publishers*, 2002.

[38] M. A. Meyers, A. Mishra, and D. J. Benson. Mechanical Properties of Nanocrystalline Materials. *Progress in Materials Science*, **51**:427–556, 2006.

[39] D.T. Britton, E.A. Odo, G.G. Gonfa, E.O. Jonah, and M. Härting. Size Distribution and Surface Characteristics of Silicon Nanoparticles. *Journal of Applied Crystallography*, **42**:448–456, 2009.

[40] N. R. Mathe. *The Rheology of Silicon Nanoparticle Inks for Screen Printing Electronic Devices*. Msc Thesis,University of Cape Town, 2009.

[41] H. Tavana and Neumann A. W. Recent Progress in the Determination of Solid Surface Tensions from Contact Angles. *Advances in Colloid and Interface Science*, **132**:1–32, 2007.

[42] D.Y. Kwok and A. W. Neumann. Contact Angle Measurement and Contact Angle Interpretation. *Advances in Colloid and Interface Science*, **31**:167–249, 1999.

[43] K. Pitt. *Handbook of Thick Film Technology*. Electrochemical Publications Ltd, Port Erin, Isle of Man, 2005.

[44] Lake Shore Cryotronics, Inc. *Hall Effect Measurement System*. http://www.lakeshore.com/sys/hall/hallmts.html, accessed on 20 December 2010.

[45] Gonfa, G. G. *Hall Effect in Printed Nanoparticulate Silicon Networks*. PhD Thesis, University of Cape Town, 2009.

[46] J. S. Kim, D. G. Seiler, and W. F. Tseng. Multicarrier Characterization on Method for Extracting Mobilities and Carrier Densities of Semiconductors from Variable Magnetic Field Measurements. *Journal of Applied Physics*, **73**:8324–8335, 1993.

[47] R. E. Hummel. *Electronic Properties of Materials*. 3rd edition, Springer-Verlag, New York, Inc., 2001.

[48] J.W. Orton and M.J. Powell. The Hall Effect in Polycrystalline and Powder Semiconductors. *Reports on Progress in Physics*, **43**:81–1297, 1980.

[49] M. Härting, J. Zhang, D.R. Gamota, and D.T. Britton. Fully Printed Silicon Field Effect Transistors. *Applied Physics Letter*, **94**:193–509, 2009.